NTNU
Norwegian University of
Science and Technology

Thermal Conductivity in PEMFC PTLs with Different Gas Content and Corresponding simple PEMFC Internal Temperature Profiles

Bjørnar Hamre

Preface

This thesis is the result of work performed from February to July 2017, with a break in May, when the author spent three weeks as an emergency substitute lecturer at the Department of Electrical Engineering and Renewable Energy at NTNU. During the first months, the author set up and programmed the experiment. Many dead-ends and much frustration are key words in describing the progress before any reliable results were produced, far overdue for the author's comfort.

The thesis was requested by the ENERSENSE research group leader, Odne Burheim (Department of Energy and Process Engineering, NTNU), who has also supervised the professional part of the project. Håvard Karoliussen (Department of Energy and Process Engineering, NTNU) has been the main supervisor and motivator for the project by constantly reminding the author of the importance of producing a solid master's thesis and the downsides of failing to do so. Robert Bock (Department of Energy and Process Engineering, NTNU) has supervised the laboratory work and participated in many a frustrating moment when things just wouldn't work properly. Morten Onsrud (Department of Materials Science and Engineering, NTNU) helped by reading through early drafts of the rapport and offering input. Fredrik Heimstad's programming skills were helpful in that he created a MATlab script for calculating and presenting the results in a satisfactory way.

Summary

More than 50 % of the PEMFC (Polymer Electrolyte Membrane Fuel Cell) energy is released as heat. The aim for this thesis was to contribute to the understanding of the management of that heat. The heat management in the PEMFC is largely controlled by the thermal conductivity of the subcomponents therein, many of which are porous to let gas and water move freely inside. It was theorised that the thermal conductivity of the gas in the porous materials contributes to a change in the total thermal conductivity in that porous region. As the anode side in a PEMFC is fully saturated by hydrogen, a gas with 7 times the thermal conductivity of air, this was an issue worth examining.

A new and roughly tested measurement apparatus was the base for what would become a measurement rig specialised to make the measurements needed to test the theory in this thesis. The programming of the control system had some complications and had an unintuitive structure. The coding was cleaned up and tests were run for materials with known thermal conductivity to make sure the rig worked properly after the clean-up in the code. A gas feed system was built to provide gas to the measurement rig in a steady and secure way. The gas feed system was implemented in the coding of the rig, after which the feed properties of the gas feed system were thoroughly explored, with and without a gas pre-heating system. Everything about the test rig that could have been affected by the newly installed gas feed system was tested again. After many failed tests and recoding sessions, the rig was deemed fully operational together with the gas feed system. The testing started and many tests were run with earlier tested materials to make sure the rig was correctly calibrated before starting the tests that produced the thesis results.

The theorised effect was proven experimentally in this thesis by measuring the thermal conductivity of two different PTL (Porous Transport Layer) materials when saturated with air and hydrogen. Argon was also used for reference. The thermal conductivity in the PTLs increased with 20 - 25 % and 10 - 15 % respectively, depending on the compaction pressure. The material with the smaller increase in thermal conductivity had a higher thermal conductivity to start with and was, therefore, less affected by the hydrogen.

Temperature profiles were made in COMSOL to prove that the change in thermal conductivity in the PTL region made a notable impact on the heat management in the PEMFC. They also proved the importance of including the thermal effect from the hydrogen gas in future models and simulations to strengthen the validity of the results from those models and simulations.

Samandrag (Norwegian Summary)

Over 50 % av energien som vert frigjort i ei PEMFC (Protonvekslande membran brenselcelle) vert frigjort som varme. Målet for denne avhandlinga var å bidra til å betra kunnskapen om korleis denne varmen oppfører seg inne i brenselcella. Korleis varmen i brenselcella oppfører seg er styrt, i hovudsak, av varmeleiingsevna til dei ulike komponentane inne i brenselcella. Mange av desse komponentane er porøse slik at gass og vatn kan flyta fritt rundt. Problemstillinga i denne avhandlinga er bygd på moglegheita for at varmeleiingsevna til gassane inne i dei porøse PEMFC-komponentane bidreg til å endra den totale varmeleiingsevna i den porøse regionen. Sidan anodesida i ei PEMFC er fullstendig metta av hydrogen, ein gas med ei varmeleiingsevne som er 7 gonger høgare enn luft, var dette ei problemstilling som var verdt å undersøkja.

Eit nytt og grovt utprøvd måleapparat var grunnlaget for det som skulle verta ein målerigg spesialisert for å gjennomføra dei målingane som var naudsynte for å kunne testa problemstillinga i denne avhandlinga. Programmeringa av kontrollsystemet hadde nokre komplikasjonar og ein lite intuitiv struktur. Det vart rydda i kodinga og køyrd testar med material med kjend varmeleiingsevne, for å sikra at riggen fungerte skikkeleg etter ryddinga i koden. Eit gassmatingssystem vart montert for å føda gass til målerigga på ein stabil og sikker måte. Gassmatingssystemet vart implementert i koden til riggen, og matingseigenskapane til gassmatingssystemet vart grundig undersøkt, med og utan eit oppvarmingssystem til gassen. Alt ved testriggen som kunne ha vorte påverka av det nyinstallerte gassmatings-systemet, vart testa igjen. Etter mange testar og små justeringar i koden, vart riggen rekna som fullt operativ saman med gassmatingssystemet. Testinga starta, og mange testar vart køyrd med tidlegare testa materiale for å sikra at riggen var riktig kalibrert før testane starta som ga resultata i denne avhandlinga.

Verknaden av gassen på den totale varmeleiingsevna i porøse brenselcellemateriale er bevist eksperimentelt i denne avhandlinga gjennom å måla varmeleiingsevna til to porøse gasstransportlag metta med luft og hydrogen. Argon vart og brukt i testinga som referanse. Varmeleiingsevna til materiala auka med respektive 20 - 25 % og 10 - 15 % avhengig av komprimeringstrykket. Varmeleiingsevna til det materialet som vart mest påverka av hydrogengassen er i utgangspunktet lågare enn i det andre materialet. Derfor vart det meir påverka av hydrogenet.

Fleire temperaturprofilar vart laga i COMSOL for å bevisa at endringa i varmeleiingsevna til den porøse regionen i brenselcella hadde stor innverknad på korleis varmen oppførte seg i brenselcella. Temperaturprofilane viste og at det vert viktig å inkludera den termiske verknaden frå hydrogenet i framtidige modellar og simuleringar for å styrka resultata frå dei modellane og simuleringane.

Nomenclature

Roman letters

A	Area	m^2
a	Tafel Constant	V
b	Tafel slope	$V \, decade^{-1}$
E	Potential	V
F	Faraday constant	$96\,485 \, C \, mol^{-1}$
G	Gibbs free energy	kJ
$\bar{g}$	Molar specific Gibbs free energy	$kJ \, mol^{-1}$
H	Enthalpy	kJ
h	Heat transfer coefficient	$W \, m^{-2} \, K^{-1}$
$\bar{h}$	Molar specific enthalpy	$kJ \, mol^{-1}$
I	Current	A
j	Current density	$A \, cm^{-2}$
j_0	exchange current density	$A \, cm^{-2}$
K_{eq}	Equilibrium constant	
P	Power	W
p	Specific power	$W \, cm^{-2}$
Q	Heat	J
$\dot{Q}$	Heat transfer	W
$\dot{q}$	Specific heat transfer	$W \, cm^{-2}$
R	Gas constant	$8.314 \, J \, mol^{-1} \, K^{-1}$
R_{el}	Electrical resistance	Ω
r_{el}	Specific electrical resistance	$\Omega \, cm^2$

R_{th}	Thermal resistance	K W^{-1}
r_{th}	Specific thermal resistance	m^2 K W^{-1}
S	Entropy	J K^{-1}
$\bar{s}$	Molar specific entropy	J K^{-1} mol^{-1}
T	Temperature	K or °C
U	Internal energy	J
v	Velocity	m s^{-1}
W	Work	J
Δx	Thickness	m
z	Number of moles electrons transferred in reaction	equiv. mol^{-1}

Greek letters

α	Symmetry coefficient	
ϵ	Emissivity	
ε	Mismatch to regression line	
η	Overpotential	V
κ	Thermal conductivity	W m^{-1} K^{-1}
σ	Stefan-Boltzmann constant	5.67·10^{-8} W m^{-2} K^{-4}

Sub- and superscripts

0	Standard
act	Activation
an	Anodic
cat	Cathodic
$cell$	Cell
con	Concentration polarisation
el	Electrical
eq	Equilibrium
r	Reaction
rev	Reversible

sc	Sample contact
ss	Stainless-steel
th	Thermal
tn	Thermoneutral
Ω	Ohmic

Abbreviations

ACL	Anode Catalyst Layer
CCL	Cathode Catalyst Layer
CL	Catalyst Layer
GDL	Gas Diffusion Layer
GUI	Graphical User Interface
HTR	Heat Transferring Rod
I/O	Input/Output
MEA	Membrane Electrode Assembly
MFC	Mass Flow Controller
MPL	MicroPorous Layer
MV	Magnetic Valve
NI	National Instruments
PEEK	PolyEther Ether Ketone
PEMFC	Proton Exchange Membrane Fuel Cell/Polymer Electrolyte Membrane Fuel Cell
PLA	PolyLactic Acid
PTFE	PolyTetraFluoroEthylene
PTL	Porous Transport Layer
SEM	Scanning Electron Microscopy
VI	Virtual Instrument
XCT	X-ray Computer Tomography

Table of Contents

List of Figures

List of Tables

Chapter 1

Introduction

In this master's thesis, thermal conductivity of porous transport layers (PTLs) has been measured when saturated with air, argon and hydrogen at room temperature to examine the issue that the thermal conductivity of the gas might affect the measured thermal conductivity in the PTL region. A thermal model has been made from assessing the internal temperature gradients in the polymer electrolyte membrane fuel cell (PEMFC) found experimentally and in earlier literature. Here follows an introduction to the thesis explaining the raised issue, its importance, and the methods used to find a satisfactory solution.

1.1   Background

International agreements like the Kyoto Protocol [1] and the more recent Paris agreement [2] have been signed to reduce environmental impacts on a global basis. 195 countries agreed on cutting CO_2 pollution to limit global warming to between 1.5 and 2.0 °C in the Paris agreement and 153 countries have ratified the agreement per July 22. 2017.[3] In large part reducing environmental impacts means phasing out the use of polluting energy sources. A major part of the energy production in the world is fossil fuel based. Fossil fuels are also dominating as energy source in the transport sector. The burning of the hydrocarbons that makes up these fossil fuels causes global environmental impacts. To reduce the need for fossil hydrocarbons for energy production and transport, cleaner fuels and technologies have to meet the demands covered by these hydrocarbons.

In phasing out fossil fuels there is a dramatic need of change in terms of resources. The resources utilised need to be renewable to have a low environmental impact, locally and globally. Most renewable energy plants have in common that the resources they exploit to produce electricity, such as wind and sunlight, are intermittent. Because of this, there is a large demand for energy buffers and resources that can be exploited at a chosen time. Fuel cells can be reversed to produce hydrogen using peak electricity for electrolysis. The energy stored in the hydrogen is in turn extracted with a fuel cell. In this way fuel cells

can be an energy buffer and help to stabilise power systems based on renewable energy sources. Fuel cells has up to this point started to enter the transport sector where they are used in hydrogen cars.

More than 50 % of the energy produced in a PEMFC is released in the form of heat.[4] To further develop and optimise the PEMFC, the understanding and management of this heat is a crucial factor. Determining thermal conductivity of the subcomponents in the PEMFC helps understand the kinetics and water management within it. Up to this point, thermal conductivity has been determined in the same way for the porous subcomponents on the anode and cathode side in the PEMFC, saturated with air. In operational mode, the PEMFC is saturated with hydrogen on the anode side. Hydrogen has a thermal conductivity 7 times higher than that of air. This thesis aims to reveal the importance of determining thermal conductivity for porous materials under the same circumstances as they would experience in an operational PEMFC. The effect of a hydrogen saturated anode region on the temperature profile in the PEMFC, is explored by determining how the thermal conductivity of air, argon, and hydrogen in a porous material affect the total thermal conductivity of that region.

1.2 Measurement rig

A specialised measurement rig is modified to determine thermal conductivity in this thesis. With the possibility of saturating a porous sample with gas during testing with a gas feed system, this rig will be used to determine thermal conductivity in gas saturated porous PEMFC materials. The rig was first assembled and used in 2016 as a part of a bachelor thesis at NTNU.[5]. The design is based on an apparatus designed and built in 2010 for determining through-plane thermal conductivity.[6]. A gas feed system is built to provide the gas for the modified measurement rig.

Chapter 2

Theory

To read this thesis and understand the need for it, the questions it asks, and how those question are answered, one need to know the theory behind the workings of the fuel cell and the methods used to analyse it. That theory is covered in this chapter after a thorough literature review of previous work on this scientific field.

2.1 Literature Review

Vie and Kjelstrup reported in 2004, in the article "Thermal conductivities from temperature profiles in the polymer electrolyte fuel cell", a large temperature gradient in the PEMFC. They found higher temperatures (5 K or more at 1 A cm^{-2}) at the membrane surface near the centre of the fuel cell than in the gas channels (see Figs. 2.4 and 2.3). This proved a significant temperature differences in the PEMFC experimentally. They suggested thermal conductivity values of 0.2 W K^{-1} m^{-1} for membranes and porous transport layers (PTLs). However, the discovered temperature gradient gave an indication that there was a great need to carry out more research on the thermal conductivity of materials used in the PEMFC.[7]

An experimental setup much like the one used in this thesis was used in the article "Direct measurement of through-plane thermal conductivity and contact resistance in fuel cell materials", from 2006. It was used there to determine the through-plane thermal conductivity (κ) of dry Nafion®, various diffusion media, catalyst layer, and the thermal contact resistance between diffusion media and a metal plate as a function of temperature and pressure. Through-plane Dry Nafion® thermal conductivity was determined to be 0.16 ± 0.03 W m^{-1} K^{-1} at room temperature, and 0.13 ± 0.02 W m^{-1} K^{-1} at 65 °C. PTL thermal conductivity was found to be a function of polytetrafluoroethylene (PTFE) content and manufacturer, and was 0.48 ± 0.09 W m^{-1} K^{-1} for untreated and 0.22 ± 0.04 W m^{-1} K^{-1} for 20 wt.% PTFE treated SIGRACET® diffusion media, respectively. Toray carbon paper PTL thermal conductivity was measured to be 1.80 ± 0.27 W m^{-1} K^{-1} at 26 °C and 1.24 ± 0.19 W m^{-1} K^{-1} at 73 °C. The thermal

contact resistance between Toray carbon paper and an aluminium bronze material was determined to drop around from $6.7 \cdot 10^{-4}$ to $2.0 \cdot 10^{-4}$ m^2 K W^{-1} for compaction pressures from 4 to 22 bar. The equivalent thermal conductivity of a 0.5 mg cm^{-2} platinum loaded catalyst layer (CL) was estimated to be 0.27 ± 0.05 W m^{-1} K^{-1}. A one-dimensional analytical model was used to estimate the temperature drop in the fuel cell components. A maximum of 3-4 K temperature drop could be expected for a 200 μm thick SIGRACET® PTL at 1.0 A cm^{-2}.[8]

It was concluded that the majority of values for thermal conductivity encountered in the earlier literature was highly overestimated in the article "Estimation of the effective thermal conductivity of carbon felts used as PEMFC Gas Diffusion Layers", from 2008. An analytical and experimental approach was used with a measurement using the same concept at the rig described in this thesis. It was focused on non-woven carbon felts that it is difficult to estimate the effective conductivity of because of the nature of heat transfer in porous and fibrous materials.[9]

The article presenting the predecessor of the measurement rig used in this thesis, "Ex situ measurements of through-plane thermal conductivities in a polymer electrolyte fuel cell" from 2010, was used to find the thermal conductivity of Nafion® membranes and SolviCore PTLs. The experimental methodology is explained there inn detail. How the thermal conductivity was affected by the wetness of the materials was explored. Thermal conductivities of Nafion membranes were measured ex situ at 20 °C to be 0.177 ± 0.008 and 0.254 ± 0.016 W m^{-1} K^{-1} for dry and maximally wetted membranes respectively. For the dry PTL at 4.6, 9.3 and 13.9 bar compaction pressures, the thermal conductivity was found to be 0.27, 0.36 and 0.40 W m^{-1} K^{-1} and the thermal contact resistivity to the apparatus was determined to be 2.1, 1.8 and $1.1 \cdot 10^{-4}$ m^2 K W^{-1}, respectively. It was shown that the thermal contact resistance between two PTLs is negligible compared to the apparatus' thermal contact resistivity. For a humidified PTL, the thermal conductivity increased by up to 70 % due to a residual liquid saturation of 25 %.[6]

The contact resistance between the GDL material and adjacent surfaces/layers was deemed as important to explore as the effective thermal conductivity in the article "Effective thermal conductivity and thermal contact resistance of gas diffusion layers in proton exchange membrane fuel cells. Part 2: Hysteresis effect under cyclic compressive load". Experiments was performed on Toray carbon papers with 78 % porosity and 5 % PTFE under a cyclic compressive load. Results showed a significant hysteresis in the loading and unloading cycle data for total thermal resistance, thermal contact resistance, effective thermal conductivity, thickness, and porosity. It was found that after 5 loading-unloading cycles, the geometrical, mechanical, and thermal parameters reached a "steady-state" condition and remained unchanged. The contact resistance was found to be the dominant contributor to the total resistance there. However, the contact resistance depends largely on the material and surface of the adjacent layers.[10]

The same research group measured in-plane thermal conductivity of GDLs one year later in the article "A novel approach to determine the in-plane thermal conductivity of gas diffusion layers in proton exchange membrane fuel cells". They found that thermal conductivity differs significantly in the through-plane and in-plane directions due to the anisotropic micro-structure of the GDL. A novel test bed that allowed separation of in-plane effective thermal conductivity and thermal contact resistance in GDLs is described in that paper. Measurements were performed using Toray carbon paper TGP-H-120 samples with varying PTFE content at a mean temperature of 65–70 °C. The in-plane effective thermal conductivity was found to remain approximately constant, $\kappa \approx 17.5$ W m^{-1} K^{-1}, over a wide range of PTFE content, and its value was about 12 times higher than that for through-plane conductivity.[11]

More in-plane measurements were carried out on different GDL materials in "Measurement of in-plane effective thermal conductivity in PEM fuel cell diffusion media". A parallel thermal conductance technique was used to determine the in-plane thermal conductivity. Conductivity values were measured at a mean sample temperature of 70 °C for six different material types and two different orientations in order to quantify the effect of PTFE content on thermal conductivity and to reveal any anisotropic behaviour. Also here the in-plane thermal conductivity was found to be 10 times that of the though-plane thermal conductivity or higher. The results varied from a minimum of $\kappa = 3.54$ W K^{-1} m^{-1} to a maximum value of 15.1 W K^{-1} m^{-1} for various samples and configurations tested in that study, with an uncertainty between 1 % and 2 % for all the cases investigated.[12]

How the thermal conductivity changed over a large temperature range was researched in "Measurement of the through-plane thermal conductivity of carbon paper diffusion media for the temperature range from -50 to +120 °C". It was found there, using the thermal capacitance method to experimentally measure the through-plane thermal conductivity of Toray carbon paper for a temperature range from -50 to +120 °C, that κ increases with higher temperatures. An earlier study [13] by the same research group found that the in-plane κ decreased at higher temperatures. The finding suggests that the thermal expansion of the carbon fibres is a direction dependent quantity.[14]

In the article "Study of thermal conductivity of PEM fuel cell catalyst layers", from 2014, the thermal conductivity of different CLs where measured both in dry and moist conditions. It was found there that the thermal conductivity of the dry CLs and the CLs with low water content proved to be between 0.07–0.11 W K^{-1} m^{-1} when compressed in the range of 5-15 bar compaction pressure. When adding water, it was observed that the water only influenced the thermal conductivity when the water content was significantly beyond the capacity of the polymer. This means that the extra water, when the ionomer is over saturated, caused the change in thermal conductivity is found in the CL. The CLs tested was found to compress almost irreversible and to be uncompressible beyond a compaction pressure of 10 bar.[15]

In "Thermal conductivity in the three layered regions of micro porous layer coated porous transport layers for the PEM fuel cell", from 2015, the composition and thermal properties of the porous transport layer (PTL) was studied. It was found there by using an X-ray computer tomography (XCT) and scanning electron microscopy (SEM) that a micro porous layer (MPL) coated PTL acts like a three-layered structure where the MPL is on one side, the PTL is on the other side, and a composite region in the middle where the two materials interacts with each other. It was found that the MPL-PTL-composite region has a much larger thermal conductivity than the two others. Therefore, the temperature drop over the composite layer could be neglected compared to the other two layers. The MPL-only layer was found to have a significantly lower thermal conductivity than the other two layers. The MPL should therefore be integrated into the GDL to reduce the temperature deviation in the PEMFC.[16]

Published review articles focusing on GDLs that can offer more insight on this scientific field and how it has advanced over the recent years are: "Gas diffusion layer for proton exchange membrane fuel cells—A review"[17] from 2009 and "Effective transport properties for polymer electrolyte membrane fuel cells–with a focus on the gas diffusion layer"[18] from 2013.

2.2 Thermodynamics

Thermodynamics is the science of heat and temperature and their relation to energy and work. The behaviour of these quantities is governed by the four laws of thermodynamics. Thermodynamics is a field of study most relevant when considering fuel cells, where heat is transported through the different materials inside. Electrochemical processes in the fuel cell are temperature dependent. Therefore, knowledge of thermodynamics associated to the electrochemistry is crucial for a deep understanding of fuel cells.

2.2.1 Thermal conductivity

Thermal conductivity, κ, is a material property and describes the material's ability to conduct heat. It is defined as the heat transfer rate through a unit thickness in a direction normal to a surface area. This is due to a unit temperature difference under steady state conditions and when heat transfer is dependant only on the temperature gradient. The heat transfer rate ($\dot{Q}$) is given in W, unit thickness, (Δx), in m, (A) is the surface area given by m^{-2}, and temperature difference, (ΔT) is given in K. Equation 2.1 explains how the thermal conductivity is calculated.

$$\kappa = \frac{\dot{Q} \cdot \Delta x}{A \cdot \Delta T} \tag{2.1}$$

The SI unit for κ is W m^{-1} K^{-1}. This means that the heat flow trough a material or a substance can be predicted if the shape and temperature drop over it is known.

κ is affected by several factors. Changes in ambient temperature and purity of the material can alter the κ significantly. When κ is given for a material, it is at an ambient temperature of 25 °C. Table 2.1 show some known values of κ for substances relevant for this thesis.

Table 2.1: Thermal conductivity of some relevant substances. [19]

Material / substance	κ at 25 $°C$ $\left[\mathrm{W\,m^{-1}\,K^{-1}}\right]$
Gases	
Air, atmosphere (gas)	0.024
Argon (gas)	0.018
Hydrogen (gas)	0.168
Oxygen (gas)	0.024
Materials	
Aluminium	205
Copper	401
Platinum	70
Steel, stainless	16
Steel (1 % carbon)	43

For entirely or mostly homogenous materials, κ is only affected by the ambient temperature. Thus we can write $\kappa = \kappa(T)$. How the thermal conductivity changes with temperature is different for each material and must therefore be determined. A trend is that κ increase with an increase in T for gases in low pressures, but it might fall or rise for metals or liquids. In Fig. 2.1 and 2.2 κ in some materials and substances are displayed as a function of temperature.[20]

It can be assessed that κ is approximately constant in a range of interest depending on the range, slope, and linearity of the function. A κ that changes linearly in the range of interest can also easily be used as a function $\kappa = aT + b$. The temperature range in this thesis is small enough to consider the thermal conductivity of the materials used constant.[20]
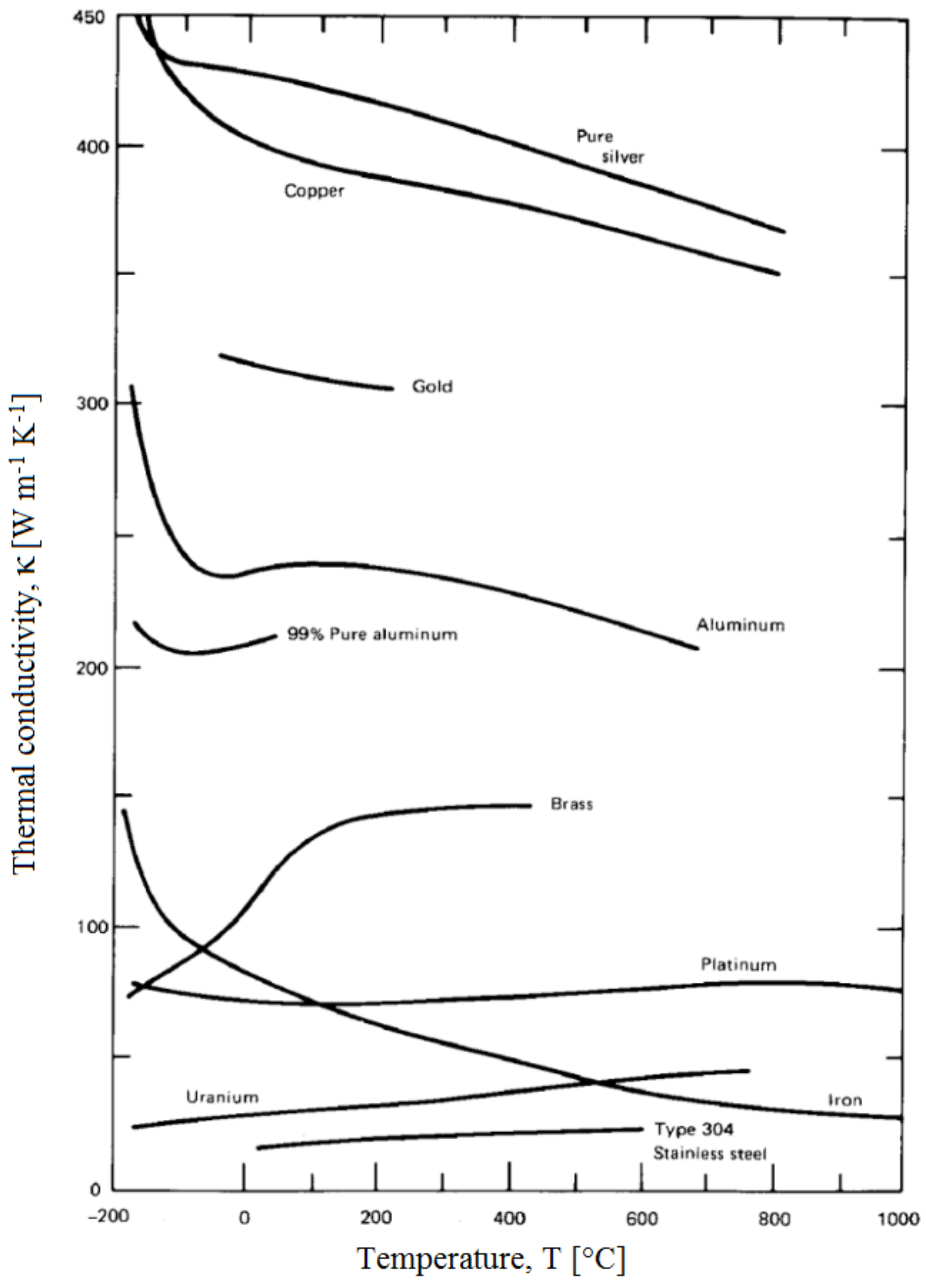
Figure 2.1: Variation of thermal conductivity in metallic solids with temperature [20]
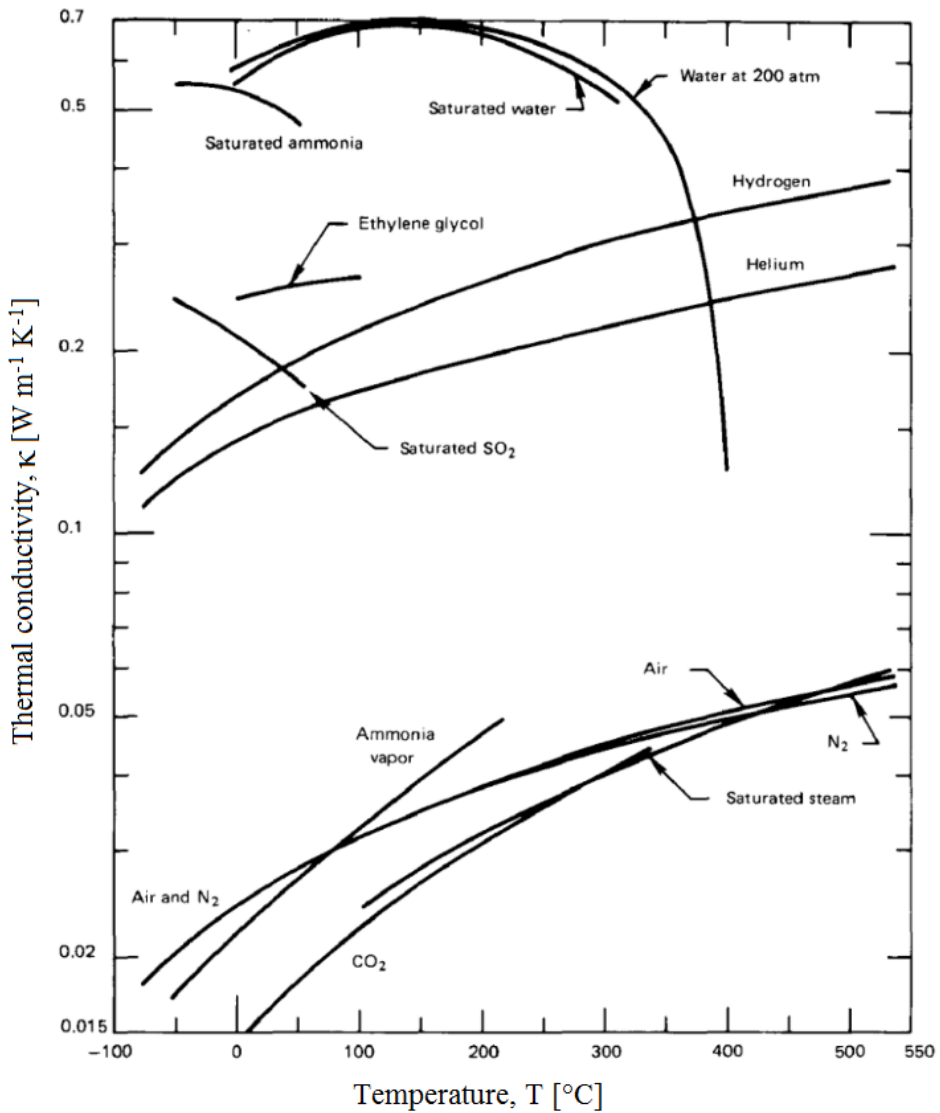
Figure 2.2: Variation of thermal conductivity as a function of temperature in liquids and gases that are either saturated or at 1 atm pressure.[20]

Specific thermal resistance, r_{th}, is the thermal conductivity inverted and shown in Eq. 2.2. This is a material property. The absolute thermal resistance, R_{th}, is not a material property. The unit is K m^2 W^{-1} for specific thermal resistance and K W^{-1} for absolute thermal resistance.

$$r_{th} = \frac{\Delta x}{\kappa} \qquad (2.2)$$

2.2.2 Energy transfer by heat

The first law of thermodynamics (TD1) constitutes that the change in the internal energy, ΔU, in a system is the sum of the heat transfer into the system, Q, and the work, W, done by the system. Equation 2.3 illustrates this. All factors have the unit for energy, J. The sign before W depends on the definition of W. If it is defined as work done by the system, it is to be subtracted. If work is done to the system, it is to be added.

$$\Delta U = Q - W \tag{2.3}$$

Heat transfer occurs between two points in space that have different temperatures. The energy transfer is always directed from the point with the higher to the point with the lower temperature. That is stated by the German scientist Rudolf Clausius' interpretation of the second law of thermodynamics. The Clausius statement from 1854 states that: *"Heat can never pass from a colder to a warmer body without some other change, connected therewith, occurring at the same time."*[21]

There are three types of heat transfer: heat conduction, convection, and radiation. More than one of the types of heat transfer can occur at a given time.[22] In a PEMFC the most relevant type of heat transfer is heat conduction. Convection may also occur in the fuel and exhaust of the fuel cell. An explanation of the different types of heat transfer follows.

CONDUCTION

Heat transfer by conduction is energy transferred between particles touching each other. Particles collide and energy transfer from the higher energy particles to the lower energy particles. Temperature measures the energy of the particles in a substance. Therefore, energy in the form of heat travel from higher temperature regions to lower temperature regions. Heat conduction occur only in solids and liquids where particles sit close enough together to touch. Fourier's law quantifies the time rate heat transfer by conduction and is explained in Eq. 2.4. $\dot{Q}$ is the heat transfer rate and measured in W. T varies linearly with the with position x. The plane A is the area normal to the measured distance, Δx, between the temperature points.[23]

$$\dot{Q} = \kappa \cdot A \cdot \frac{\Delta T}{\Delta x} \tag{2.4}$$

CONVECTION

Heat transfer by convection is the energy transfer between a solid surface with a given temperature and an adjacent gas or liquid with another temperature. The rate of energy transfer between the fluid and the surface can be quantified using Eq. 2.5, also known as Newton's law of cooling. h is the heat transfer coefficient and A is the surface area in contact with the fluid. The heat transfer coefficient is an empirical proportionality factor that includes the flow pattern near the surface, the fluid properties and the geometry. A moving fluid generally means a higher heat transfer coefficient. Fans or pumps are often

used to move the fluid to increase the heat transfer. This is called forced convection. Otherwise the convection is called free. Typical heat transfer coefficients values are shown in Tab. 2.2. The heat transfer coefficient is clearly higher for liquids than for gases. That is because of the difference in density of the different phases.[23]

$$\dot{Q} = h \cdot A \cdot \Delta T \tag{2.5}$$

Table 2.2: Typical heat transfer coefficient values. [23]

Applications	h at $25\,°C\,[W\,m^{-2}\,K^{-1}]$
Free convection	
Gases	2 - 25
Liquids	50 - 1 000
Forced convection	
Gases	25 - 250
Liquids	50 - 20 000

The convecting heat transfer of air is can be calculated to an approximate value by Eq. 2.6,where v is the relative speed of the object through the air in m s^{-1}.[19]

$$h = 10.45 - v + 10v^{0.5} \tag{2.6}$$

RADIATION

Thermal radiation is the result of changes in the electronic configuration of atoms or molecules in a matter. The energy is transported by photons and does not rely on any intervening medium. All matter emits radiation to varying degrees. The rate of the energy transfer from a surface area A with the temperature T is macroscopically quantified in Eq. 2.7, a modified version of the Stefan-Boltzmann law. ϵ is the emissivity, a property of the surface that indicates how efficiently it emits radiation. It is always between 0 and 1. σ is the Stefan-Boltzmann constant. Because of the small size of the Stefan-Boltzmann constant, the energy transfer from radiation does not become of any practical relevance without a significant temperature difference.[23]

$$\dot{Q} = \epsilon \cdot \sigma \cdot A \cdot T^4 \tag{2.7}$$

when T is the surface temperature. If $T \approx T_{surroundings}$, Eq. 2.7 can be rewritten as Eq. 2.8, where $\Delta T = T - T_{surroundings}$.

$$\dot{Q} = \epsilon \cdot \sigma \cdot A \cdot T^3 \cdot \Delta T \tag{2.8}$$

2.3 The PEMFC

Fuel cells are galvanic cells, in which the free energy of a chemical reaction is converted into electrical energy through an electrochemical reaction. The Gibbs free energy change of the chemical reaction is related to the cell voltage as seen in Eq. 2.9. The Gibbs free energy is here mole specific and has the unit J mol^{-1}.[24]

$$\Delta \bar{g}^0 = -zFE^0 \tag{2.9}$$

where z is the number of moles electrons involved in the reaction, F is the Faraday constant, and E^0 is the voltage of the cell for thermodynamic equilibrium in the absence of a current flow, also called standard cell potential. The anode reaction in fuel cells is the direct oxidation of hydrogen (or of methanol in the case of a direct methanol fuel cell). An indirect oxidation via a reforming step can also occur. The cathode reaction in fuel cells is oxygen reduction, in most cases from air. The principle for the PEMFC and other hydrogen/oxygen fuel cells is shown in Fig. 2.3. The anode reaction in the PEMFC is shown in Eq. 2.10 and the cathode reaction, where the product is liquid water, is shown in Eq. 2.11. The overall reaction for when the product of the reaction is liquid water is explained in Eq. 2.12, where $\Delta \bar{g}^0$ = -237 kJ mol^{-1} when the reaction product is liquid water. If the product of the reaction is steam, the reaction is the same but has a lower free energy, $\Delta \bar{g}^0$ = -229 kJ mol^{-1}.[25]

$$H_{2(g)} \rightarrow 2H^+_{(aq)} + 2e^- \tag{2.10}$$

$$\frac{1}{2}O_{2(g)} + 2H^+_{(g)} + 2e^- \rightarrow H_2O_{(l)} \tag{2.11}$$

$$H_{2(g)} + \frac{1}{2}O_{2(g)} \rightarrow H_2O_{(l)} \tag{2.12}$$
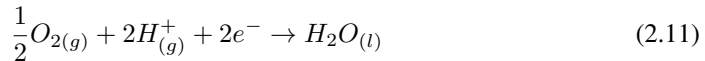
By running a current through some fuel cells, the reaction in Eq. 2.12 is reversed and fuel cells produce hydrogen through electrolysis. This is possible in a PEMFC. Figure 2.3 illustrates how a PEMFC works. Hydrogen gas travels through a porous carbon layer to the catalyst layer where the anode reaction takes place. The electrolyte only lets through hydrogen ions. Oxygen gas reach the catalyst layer on the cathode side where it reacts with the hydrogen ions in the cathode reaction. The excess electrons on the anode side powers a current in an external circuit.
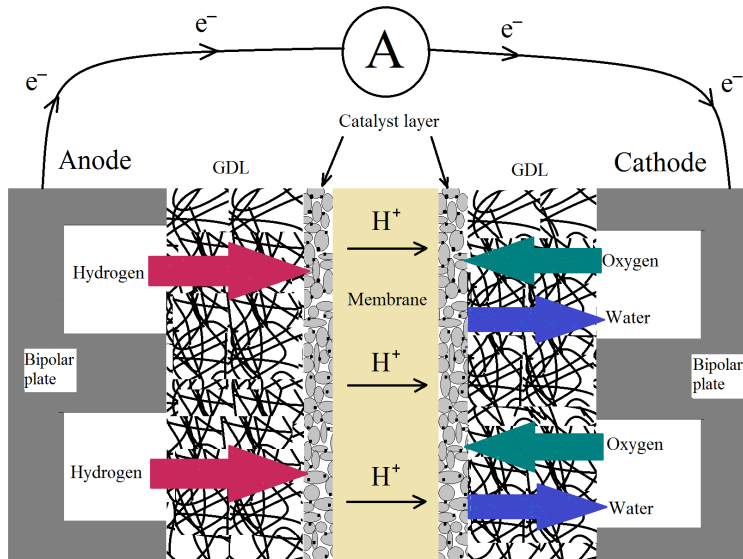
Figure 2.3: Schematic illustration of a PEM fuel cell.

There are many types of fuel cells; Alkaline Fuel Cell (AFC), Proton Exchange Membrane Fuel Cell (PEMFC), Direct Methanol Fuel Cell (DMFC), Phosphoric Acid Fuel Cell (PAFC), Molten Carbonate Fuel Cell (MCFC) and Solid Oxide Fuel Cell (SOFC). The basic differences are the electrolyte used, their operating temperature, their design, and their field of application. Moreover, each type has specific fuel requirements. The only fuel cell focused on in this thesis is the most common PEMFC.[26]

2.3.1 PEMFC Components

The PEMFC consists of several components. Each component is developed to perform one or more task optimally in the fuel cell. The components are the catalyst layer (CL), the micro porous layer (MPL) and porous transport layer (PTL) on each side of a membrane. The MPL and PTL combined are often called the gas diffusion layer (GDL). Bipolar plates enclose the assembly. A complete membrane electrode assembly (MEA) is explained in Fig. 2.4.
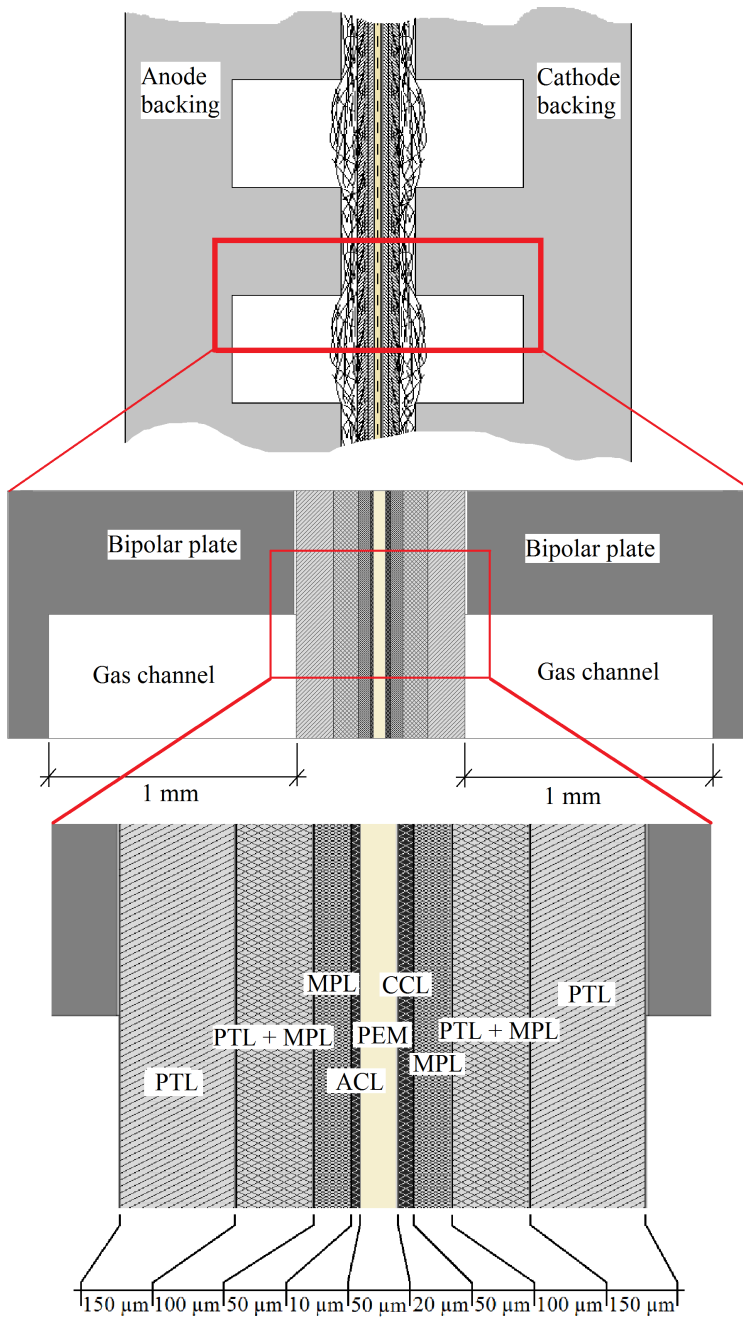
Figure 2.4: Full MEA geometry (top). Geometry of the MEA region used for COMSOL modelling (middle). Geometry of PEMFC components between bipolar plates (bottom).

POROUS TRANSPORT LAYER

The PTL transport fuel gases from gas channels in the bipolar plates to the MPL and waste gas and water the other way. It is made of conducting porous carbon materials like carbon cloth or carbon paper. The PTL is an elastic component necessary for the fuel cell to handle the compression needed to establish good contact.[27] When the MPL is coated on the PTL, the interface between the PTL and MPL achieves new properties.[16] When in operating mode, the PTL is saturated with either hydrogen or oxygen/air depending on if it is the anode or cathode side. The PTL-MPL interface region and the MPL also contains the fuel gases and could be affected by this.

PTL–MPL INTERFACE

In the interface region between the PTL and the MPL the smaller particles of the MPL enters in between the larger particles of the PTL and makes the area more compact. This region is considered its own region in thermal studies when modelling is used because of its differing properties from the PTL and MPL.[16]

MICRO POROUS LAYER

The MPL was initially made to support the CL.[28] However, the MPL has been shown to play an important part of the water removal in the PEMFC. It sits between the PTL and the CL. The MPL are often coated with a CL in manufacturing. The MPL consists of carbon black powder and a hydrophobic agent. This provides the right surface pore size and keeps the CL from flooding.[27]

CATALYST LAYER

Platinum is considered the best catalyst for both the anode and the cathode even though they rely on completely different reactions. The cathode requires more platinum than the anode, but often the same amount is used to simplify the setup. Small platinum particles are spread on the surface of larger carbon powder particles. In this way, the catalyst is spread over a large surface area where it is in contact with the reactants.[27] The anode catalyst layer (ACL) is on the anode side of the membrane and the cathode catalyst layer (CCL) is on the cathode side. As seen in Eq. 2.11, the product of the cathode reaction is water. This water is lead away from the fuel cell to not block the gas flow to the CL. At the start-up of the PEMFC technology platinum was used to the rate of 28 mg cm^{-2}. The content has decreased to around 2 mg cm^{-2} in later years. See also Fig. 2.3 where the catalyst layer is enhanced to a state where black platinum particles can be seen attached to the larger grey carbon particles.[27]

<u>MEMBRANE</u>

In a PEMFC the membrane is proton exchanging. PEM spells out proton exchange membrane. The proton is a positively charged hydrogen ion and is the charge-bearing ion in the fuel cell that creates the potential for the outer circuit. Therefore, the membrane's ability to transport the charge bearing ion must be good, but the membrane also needs to keep the reactants separated for the PEMFC to perform. To force electrons into using an outer circuit, the membrane is made from a non-electron-conducting material. If it is conducting, the PEMFC will short circuit. The most used membranes in PEMFCs are Nafion®️ membranes and PTFE-Nafion®️ composite membranes. Nafion®️ membranes have better ion conductivity but the composite membrane have more mechanical strength and better thermal stability. Nafion®️ has a chemical structure with a hydrophobic tetrafluoride backbone and hydrophilic sidechains.[29]

<u>BIPOLAR PLATES</u>

The biploar plates, often called flow fields, have channels engraved in them for the transport of gas and water to and from the GDL. The pattern of the channels is made optimal for an even distribution of feed gas and effective water removal. As explained, water is the product of the cathode reaction. They have high electrical conductivity to efficiently transport electrons from the anode and to the cathode.

2.4 Heat Production in PEMFC

As the PEMFC is used to produce electricity from hydrogen, all heat that is produced form the operation is considered a loss. Heat is produced near the middle of the MEA by ohmic resistance and other overpotentials present when the chemical energy in hydrogen force a current of ions from the anode to the cathode side of the MEA. The different reasons for heat production in the PEMFC are explained more in detail in this chapter.

2.4.1 Thermodynamic relations

Considering the fuel cell as an open thermodynamic control volume, a version of the first law of thermodynamics can be used:

$$\Delta H = Q - W \tag{2.13}$$

where the enthalpy (ΔH) increase if heat (Q) is added to the control volume and decrease if work (W) is extracted. All elements in the equation have the unit J. For an open fuel cell under reversible conditions, the electric work can be expressed by the product of the current, I, and the voltage E_{rev}. The current is the quantity of electric charge per unit of second and thus can be expressed by Faraday's law (see Eq. 2.14) where n is the number of moles of reactant, t is time, z is the number of moles of electrons per mole reactant, and F is Faraday constant that represent the charge of one mole of electrons. Mostly, current

density, j, is used instead of absolute current when considering fuel cells. Current density is area specific (often with the unit A cm^{-2}) and is therefore a better measurement of the quality of the fuel cell as it is not dependent on the size of the system.

$$n = \frac{It}{zF} \tag{2.14}$$

Under reversible conditions, the entropy change in the fuel cell directly relates to the reversible heat exchange.

$$Q_{rev} = T\Delta S \tag{2.15}$$

where ΔS is the reaction entropy. ΔG is the amount of available work from the reaction and, therefore, the total energy in the reaction can be written as:

$$\Delta H = T\Delta S + \Delta G \tag{2.16}$$

and with the definition of Gibbs free energy in a chemical reaction explained in Eq. 2.9, Eq. 2.13 becomes Eq. 2.17, where $\Delta \bar{h}$ and $\Delta \bar{s}$ are the mole specific values of ΔH and ΔS.

$$\Delta \bar{h} = T\Delta \bar{s} - zFE_{rev} \tag{2.17}$$

Cell potential is defined at standard conditions. At standard conditions, the temperature is 298 K and the pressure is 1 bar. Reversible potential in electrochemistry is calculated by Nernst equation shown in Eq. 2.18. It is an expression of the maximum possible open-circuit (zero-cell-current) voltage as a function of temperature and pressure and is an expression of an established thermodynamic equilibrium. For the reversible reaction in a fuel cell, $E_{rev} = E^0 = 1.23$ V at standard pressure, temperature and pH=0.[30, 31]

$$E_{rev} = E^0 - \frac{RT}{zF}ln(Q_r) \tag{2.18}$$

where R is the gas constant and Q_r is the reaction quotient defined as shown in Eq. 2.20 from the made up reaction in 2.19, where substances A and B are reactants, C and D are products, and α, β, γ, and δ are the number of moles of the substances in the reaction.

$$\alpha A + \beta B = \gamma C + \delta D \tag{2.19}$$

$$Q_r = \frac{C^\gamma D^\delta}{A^\alpha B^\beta} \tag{2.20}$$

At equilibrium state $\Delta\bar{g} = 0$ and $Q_r = K_{eq}$. This leads to Eq. 2.21.

$$\Delta\bar{g}^0 = -RTln\left(K_{eq}\right) \tag{2.21}$$

where K_{eq} is the equilibrium constant that, for ideal gases, represents the ratio between the concentration of the products and the concentration of reactants at equilibrium state.

Figure 2.5 illustrate the influence of temperature on the standard cell potential per Eq. 2.17, as the relation is likewise for standard values.
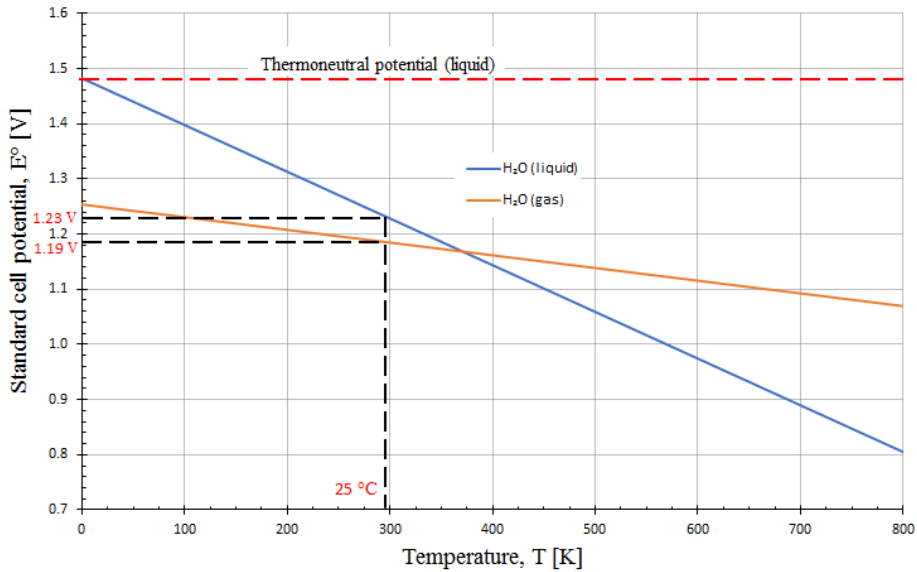
Figure 2.5: Influence of temperature on standard cell potential according to Nernst equation.

For the PEMFC, ΔS is negative and relatively large. This is because gases have much larger ΔS than liquids and also that there are fewer moles of substance after the reaction. When water is formed in liquid state, more energy is produced in the fuel cell than if the water was formed in gas form. This is because water use energy when it evaporates and release energy when it condensate.

Another important physical quantity for PEMFC is the thermoneutral potential shown in Eq. 2.22.

$$E_{tn} = -\frac{\Delta H}{zF} \tag{2.22}$$

The thermoneutral potential represents the total energy potential in the reaction in the fuel cell for the work and heat. Multiplied by the current density, it expresses the total specific power production in the cell as seen in Eq. 2.23. The electrical power as well as the released heat flow. The thermoneutral potential for liquid water is 1.48 V. For steam, thermoneutral potential is 1.25 V.[31]

$$E_{tn}j = p_{el} + \dot{q} \tag{2.23}$$

p_{el} in Eq. 2.23 is the area specific electrical power and $\dot{q}$ is the area specific heat transfer. According to the definition of Gibbs free energy, thermoneutral potential can now be expressed as in Eq. 2.24.

$$E_{tn} = E_{rev} - \frac{T\Delta S}{zF} \tag{2.24}$$

If the theoretical hypothesis of reversible conditions is removed to create a more realistic scenario, a current flow through the system and electric work is delivered. The total entropy change is no longer zero and the heat production increase. Other losses appear due to the current flowing in the system. These losses are called overpotentials and further reduce the potential of the cell, E_{cell} and creates more heat. With a current flowing through the cell, Ohm's law (Eq. 2.25) must be considered and the cell potential is split into reversible potential and overpotentials as shown in Eq. 2.26.

$$E = IR_{el} \tag{2.25}$$

$$E_{cell} = E_{rev} + r_{el}j + \eta_{an} + |\eta_{cat}| \tag{2.26}$$

where r_{el} is the symbol for specific electrical resistance with the unit $\Omega\,m^2$. Therefore, $r_{el}j$ represent the ohmic losses in the materials due to the current flow through it and η_{an} and η_{cat} represent the overpotential at the anode and cathode side. The overpotentials are experienced as losses because part of the available energy is used to produce potentials that are unextractable as work. Figure 2.6 illustrate the relations between the thermodynamics and the electrical potentials in an electrochemical cell.

With losses introduced, electrical power and heat flow can be expressed respectively by Eq. 2.27 and 2.28.

$$p_{el} = E_{cell}j = -\frac{\Delta G}{zF}j - \eta j - r_{el}j^2 \tag{2.27}$$

$$\dot{q} = -\frac{T\Delta S}{zF}j + \eta j + r_{el}j^2 \tag{2.28}$$
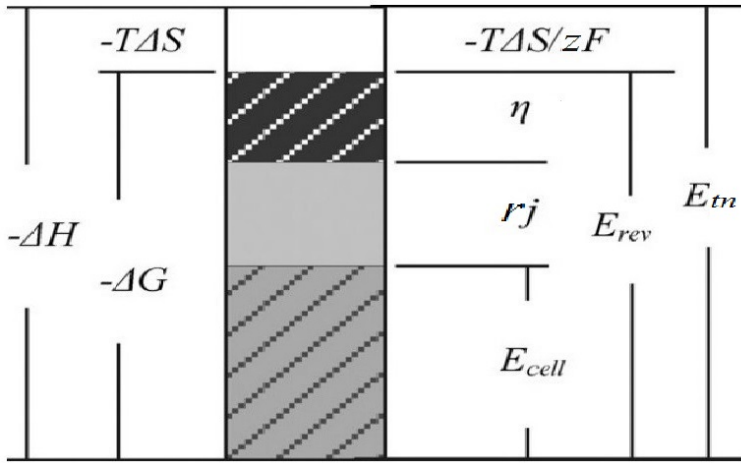
Figure 2.6: Relations between the thermodynamics and the electrical potentials in an electrochemical cell.[32]

POLARIZATION CURVE

In Fig. 2.7, a typical PEMFC polarization curve is represented in a plot. It shows the relation between the current density and the cell voltage. The polarization curve is widely used to establish the performance of fuel cells.
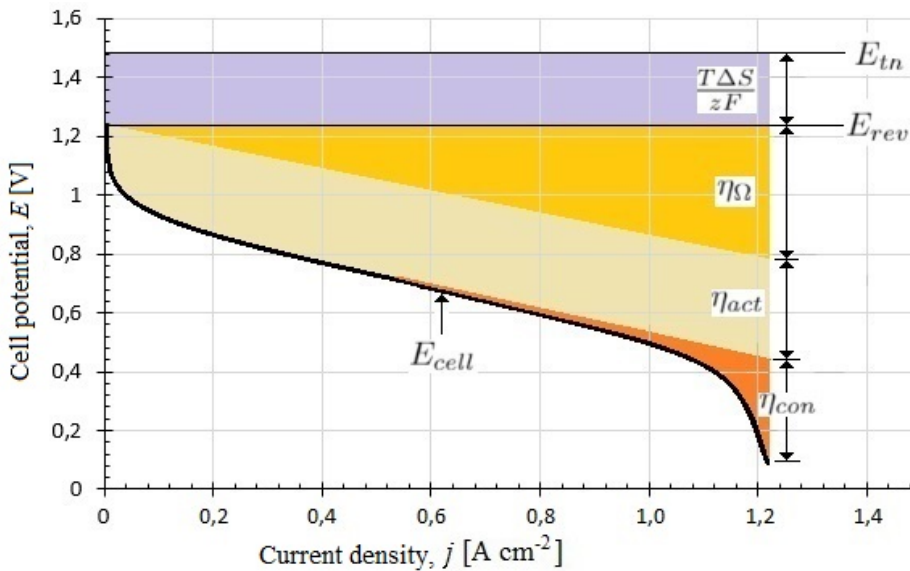
Figure 2.7: Polarization curve that show the cell potential as a function of the current density and the contributing overpotentials.

The first part of the polarization curve is influenced by activation loss, called the activation overpotential (η_{act}), that occurs when a small current starts flowing and the kinetics of the electrochemical reaction is slow. The energy required for the activation can be seen as an obstacle that reactants has to overcome for starting the reaction. The process operates away from equilibrium and there is a net current. The anodic current becomes larger than the cathodic current. This difference between the currents results in a friction beyond the ohmic potential. i.e. there is a potential change due to the friction of exchanging electrons faster than the equilibrium rate. This type of loss is negatively exponential. It grows rapidly with the current density when it is relatively low, before gradually reaching a constant value. In a PEMFC this type of losses occurs mostly at the cathode due to the kind of mechanism of reaction involved.[33]

In the central part of the polarization curve, the fuel cell is subjected to ohmic losses, η_Ω. As for every device in which a current flow, also a fuel cell is subjected to an ohmic potential drop. This loss has a linear trend that derives from the Ohm's law (Eq. 2.25). All the materials in the fuel cell with a current flowing through them provide ohmic losses. Both the electrons in the electrodes and the protons in the membrane experience this. The membrane is playing a very important role for the determination of the ohmic losses. Operative temperature of the cell and the hydration of the membrane influences the resistance of the membrane. The transport of the protons through the polymer occurs because of the presence of the molecules of water that forms ions of big dimensions.

The mass transport losses, or concentration polarization losses, occur at high current densities when the diffusion of the reactant through the catalyst layer limits the power exploited by the cell. High current densities lead to more charged particles flowing per second and hence, a high reaction rate. The mass transport of the reactants is now the reason of the decline in the power generated. One of the methods to reduce this type of losses is to run the fuel cell with pure reactants. The mass transport to the electrode runs more smoothly when there is no need for diffusion inside the gas flow. The electrical potential loss caused by these losses is called the concentration polarization overpotential, η_{con}.

BUTLER-VOLMER EQUATIONS

Electrode equilibrium currents can be expressed for the anode and cathode by Eqs. 2.29 and 2.30.

$$j_{an} = j_0 \, exp \left[\frac{(1-\alpha)zF}{RT} \eta_{an} \right] \tag{2.29}$$

$$j_{ca} = -j_0 \, exp \left[\frac{\alpha zF}{RT} \eta_{cat} \right] \tag{2.30}$$

where j_0 is the exchange current density and α is the symmetry coefficient. The exchange current density is the reaction rate when kinetic equilibrium occurs. The symmetry coefficient express whether the electrode reaction is favoured in one direction or not. If $\alpha = 0.5$, no reaction is favoured.

Combining Eqs. 2.29 and 2.30, the Butler-Volmer equation is obtained (Eq. 2.31).

$$j = j_0 \left(exp \left[\frac{(1 - \alpha)zF}{RT} \eta_{an} \right] - exp \left[\frac{\alpha zF}{RT} \eta_{cat} \right] \right) \tag{2.31}$$

Looking at Eq. 2.31, one can see that there are two contributions to the reaction rate. One is the product formation (anode) reaction and the other is the reactant formation (cathode) reaction. The overall current, j, is limited by the reactant formation. For large overpotential values, the product reaction can be neglected. Neglecting this term, the Butler-Volmer equation is simplified Eq. 2.32 where only the overpotential on the anode is included.

$$j = j_0 \; exp \left[\frac{(1 - \alpha)zF}{RT} \eta_r \right] \tag{2.32}$$

where $\eta_r = \eta_{an} = -\eta_{cat}$. The overpotential can now be found using the Tafel equation, Eq. 2.33, a simpler approach to the Butler-Volmer equation. It is valid for all but very small current densities.

$$\eta_r = a + b \; log j \tag{2.33}$$

Factors a and b are explained in Eqs. 2.34 and 2.35. b is negative for the cathode.

$$a = -\frac{RT}{\alpha F} log j_0 \tag{2.34}$$

$$b = \frac{RT}{\alpha F} \tag{2.35}$$

How the Tafel overpotential relates to the Butler-Volmer overpotential in the activation area, is illustrated in Fig. 2.8. The Tafel approximation in the plot differs at small current densities, but can be used accurately at higher current densities.
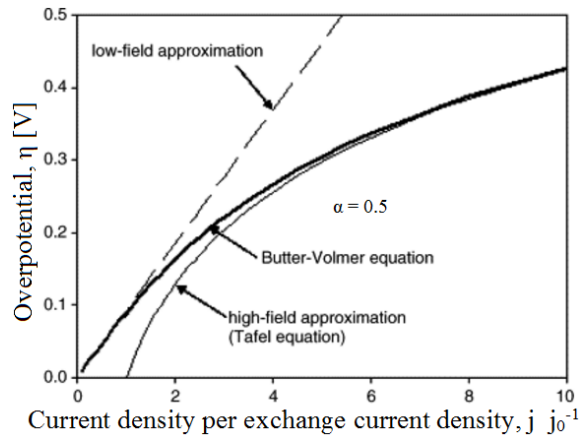
Figure 2.8: Plot of a typical Tafel and Butter-Volmer activation overpotential as a function of current density.[33]

2.5 Software Tools

Software tools used in the thesis are introduced here.

2.5.1 LabView

LabView is a systems engineering computer software from National Instruments (NI) that provides test measurements and control with rapid access to hardware and data insights. It integrates hardware so that one can acquire and visualise data sets from an input/output (I/O) device, from NI or a third party. LabView uses graphical programming where graphical blocks are used to communicate with hardware, carry out calculations, and collect, write, and save information. A graphical user interface (GUI) called the front panel is used to access and control information from the block diagram. The front panel is designable and is set up to make the controlling of a program intuitive and lucid with graphs, lights, buttons, and other indicators and controls. A LabView program is called a Virtual Instrument (VI).[34]

For running experiments where measurements are taken continuously over a longer period, using LabView can save much effort and many work hours. A highly complex experiment can be made quite simple if LabView is used correctly. Optimally, one would press the run button on the front panel and the VI would carry out the complete experiment, and process the collected data to make it presentable directly. However, the more task one gives LabView to carry out, the more complex the code becomes, and higher expertise is required from the person writing the code. It can therefore be considered important to put down some extra work into the code, making it as simple and intuitive as possible. This can save many hours of troubleshooting in the long run.

2.5.2 COMSOL

COMSOL Multiphysics® is a comprehensive simulation software. It includes multiple scientific models that considers the effect of fluids, heat and mechanics. COMSOL Multiphysics® includes the COMSOL Desktop® GUI and a set of predefined user interfaces with associated modelling tools, referred to as physics interfaces, for modelling common applications. Complex systems of any geometry can be modelled. Material properties for the materials used in the model are set as globally defining parameters. A calculation mesh is set up to decide the solution of the calculations. Heat sources and sinks are decided in the case of heat transfer modelling. Results are presented directly as graphs and plots, or as datasheets to be exported and processed by another software.[35]

Presenting a model that is self-explanatory or easy to recognise and understand is very important in a research rapport. COMSOL calculate and present such models at a high level. Colourful figures and plots in 2D or 3D capture the eye and can explain effects that otherwise would demand hours of reading heavy theory to understand. Objects drawn in CAD software can be imported into COMSOL Multiphysics® where it can be set up as a model exposed to a vast number of effects. These effects span from chemical effects through mechanics, acoustics, fluid and heat to electromagnetics.

2.6 Calculation Formulas

Some of the mathematics used to calculate the thesis results is explained here.

2.6.1 Error propagation

The error propagation for the reported values is calculated using the propagation of error formula. The formula is displayed in Eq. 2.36.[36]

$$S_x^2 = \left(\frac{\partial x}{\partial a} \cdot S_a \right)^2 + \left(\frac{\partial x}{\partial b} \cdot S_b \right)^2 + \left(\frac{\partial x}{\partial c} \cdot S_c \right)^2 \tag{2.36}$$

where S_x is the standard deviation for the reported value x. S_a, S_b, and S_c are the standard deviations for the measurements x is based on.

κ is calculated using Eq. 2.2, where the propagation of error for the thermal resistance is described in Eq. 2.37.[36]

$$S_{r_{th}}^2 = \left(\frac{\partial r_{th}}{\partial \Delta T} \cdot S_{\Delta T} \right)^2 + \left(\frac{\partial r_{th}}{\partial \dot{q}} \cdot S_{\dot{q}} \right)^2 \tag{2.37}$$

where the standard deviation for $\dot{q}$ was calculated using Eq. 2.38.

$$S_{\dot{q}}^2 = \left(\frac{\partial \dot{q}}{\partial \kappa_{ss}} \cdot S_{\kappa_{ss}} \right)^2 + \left(\frac{\partial \dot{q}}{\partial \Delta x} \cdot S_{\Delta x} \right)^2 + \left(\frac{\partial \dot{q}}{\partial \Delta T} \cdot S_{\Delta T} \right)^2 \qquad (2.38)$$

where $S_{\kappa_{ss}}$ is the standard deviation for the thermal conductivity of the steel rod, $S_{\Delta x}$ is the standard deviation for the distance between the thermocouples in the steel rod and $S_{\Delta T}$ is the standard deviation of the temperature difference.

2.6.2 Least Square Regression

The thermal conductivity is found using the slope of the function seen in Eq. 2.47. When using least square regression to calculate that trend line, a factor is added to the function that is used to calculate variance of the other regression coefficients (see Eq. 2.39). ε_i is the $r_{th,i}$ value mismatch to the regression line and is attributed to measurement errors.[37]

$$r_{th,i} = \frac{1}{\kappa} \Delta x_i + 2 \cdot r_{contact} + \varepsilon_i \qquad (2.39)$$

The regression coefficients $\frac{1}{\kappa}$ and $2 \cdot r_{contact}$ are given by Eqs. 2.40 and 2.41.[37]

$$\frac{1}{\kappa} = \frac{\sum_{i=1}^n \left(\bar{r}_{th} - r_{th,i} \right) \left(\Delta \bar{x} - \Delta x_i \right)}{\sum_{i=1}^n \left(\Delta \bar{x} - \Delta x_i \right)^2} \qquad (2.40)$$

$$2 \cdot r_{contact} = \bar{r}_{th} - \frac{1}{\kappa} \Delta \bar{x} \qquad (2.41)$$

where $\bar{r}_{th}$ and $\Delta \bar{x}$ are the averages of all the $r_{th,i}$ and Δx_i values. Standard deviation of the regression coefficients are found through ε. By rearranging Eq. 2.39 ε is calculated (see Eq. 2.42).

$$\varepsilon_i = r_{th,i} - \frac{1}{\kappa} \Delta x_i + 2 \cdot r_{contact} \qquad (2.42)$$

Variance of the thermal resistance values is then found in Eq. 2.43.[37]

$$s_{r_{th}}^2 = \frac{\sum_{i=1}^n \varepsilon_i^2}{n - 2} \qquad (2.43)$$

The variance of the thermal resistance is in turn used to calculate the variance of the regression coefficients in Eqs. 2.44 and 2.45.[37]

$$s^2_{\frac{1}{\kappa}} = s^2_{r_{th}} \frac{1}{n \sum_{i=1}^{n} (\bar{x} - x_i)^2} \tag{2.44}$$

$$s^2_{2 \cdot r_{contact}} = s^2_{r_{th}} \frac{\sum_{i=1}^{n} x_i^2}{n \sum_{i=1}^{n} (\bar{x} - x_i)^2} \tag{2.45}$$

2.7 Thermal Conductivity from Thermal Resistance

The thermal resistance between the thermocouples on each side of the sample or stack is calculated using Eq. 2.2. However, the calculated thermal resistance is actually the thermal resistance of the sample/stack plus the thermal contact resistance on each side of the stack. The relation is explained in Eq. 2.46. The contact thermal resistance between the aluminium cap and the sample is then deconvoluted from the thermal resistance of the sample by plotting the total thermal resistivity as a function of the stack thickness, Δx. Comparing Eq. 2.2 and Eq. 2.4, a new equation, Eq. 2.47, can be contrived to show that the inverse of the slope in that plot is the thermal conductivity.[16]

$$r_{th} = r_{th,sample} + 2 \cdot r_{contact} \tag{2.46}$$

$$r_{th} = \frac{1}{\kappa} \cdot \Delta x + 2 \cdot r_{contact} \tag{2.47}$$

This calculated thermal conductivity however, may contain hidden factors not accounted for. The sample thickness is increased by stacking several samples on top of each other. By doing so, there is an additional thermal contact resistance introduced [9]. The sample/stack thermal resistance is then deconvoluted into Eq. 2.48.

$$r_{th,stack} = n \cdot r_{th,sample} + (n-1) \cdot r_{sc} \tag{2.48}$$

where n is the number of samples, $r_{th,sample}$ is the thermal resistance of a single sample, and r_{sc} is the thermal contact resistance between each sample in the stack. The challenge is then to differentiate between the two thermal resistances because they are linearly dependent. Another way of explaining this is that adding another sample in a stack does not add a new equation to the list of unknowns. To deal with this problem one either needs to demonstrate that the sample-sample resistance is negligible or one needs materials that come in different thicknesses so that the sample-sample resistance is no longer present. In this thesis, the possibility of an additional resistance, r_{sc}, to be influential on the final results is considered negligible and therefore discounted. Thermal contact resistance is included in COMSOL as a 10 μm air/gas gap the in COMSOL.[16].

Apparatus

The Apparatus, or measurement rig, used to measure thermal conductivity for PTLs was of absolute importance for this thesis as the results are based solely on those measurement data and the comparing of them to known values found in earlier literature.

3.1 The measurement rig

The rig is depicted in Figs. 3.1 and 3.2. Peltier modules create a directed heat flow forced to run through the test sample. The size of the heat flow is controlled by adjusting the voltage over the Peltier modules. Stainless-steel rods, called heat transfer rods (HTRs), press down on the sample to direct the heat through the sample. Two micrometers measure the thickness of the sample between the stainless-steel rods. Thermocouples measure temperatures in different locations in the rods and aluminium caps to determine the heat flux through the sample using Eq. 2.4, as well as the temperature drop over the sample. When the heat flow through the two steel rods are the same, it is also equal to the heat flow in the sample. Thermal resistance between the thermocouples is calculated with Eq. 2.2.

An outer frame in stainless steel, and the rods in the same material, makes the rig's framework have good tensile strength. The pressure in the sample is contrived by a pneumatic plunger lifting the lower part of the rig, pressing the two steel rods towards each other. The handle seen on top of the rig in Fig. 3.2 lifts the upper part of the rig from the lower part between test so that it is possible to change the sample. The handle locks when lifted so that the upper part of the rig stays up when lifted. By pushing a bolt, the upper part can be lowered again.
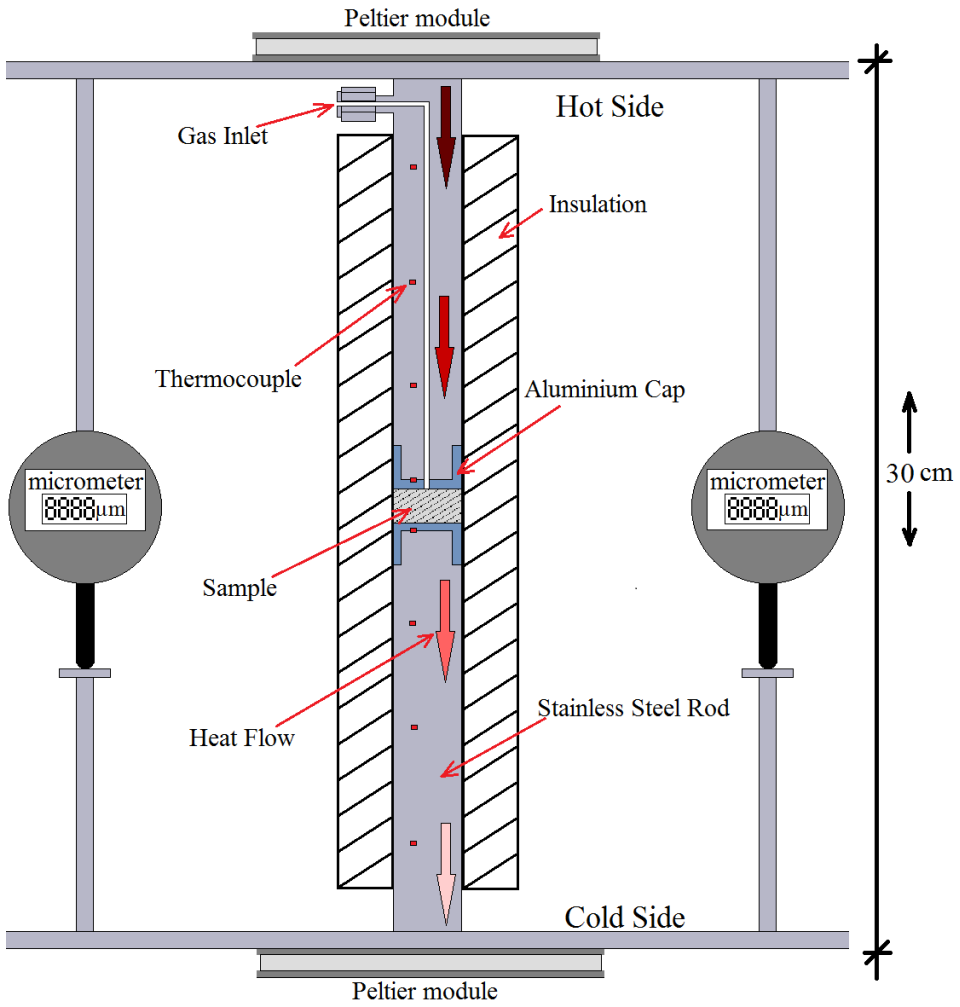
Figure 3.1: Schematic depiction of the test rig used to measure thermal resistance. Eight thermocouples measure the temperatures through the heat transfer rods while the micrometers measure the thickness of the sample.
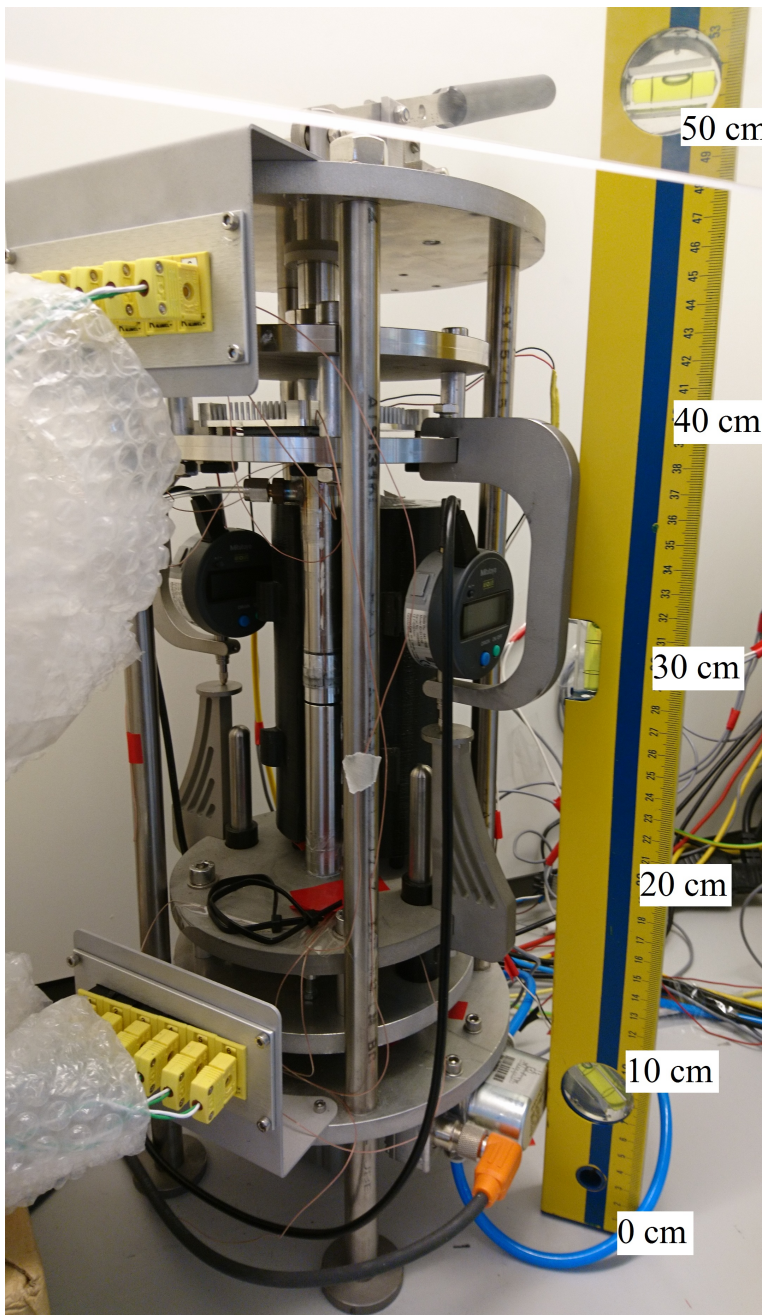
Figure 3.2: The measurement rig depicted in the fume hood without the insulation capsule.

3.1.1 Peltier Thermoelectric Modules

Thermoelectric Peltier modules use electricity to create a temperature difference with the Peltier effect. The Peltier effect is the presence of heating or cooling at an electrified junction of two different conductors.[38] Originally, two Peltier modules was used to create the heat flow in the test rig. However, the temperature difference from room temperature to the hot side was much larger than that between room temperature and the cold side. As the tests was to be carried out at room temperature, these temperature difference should be equally large. The effect of adding a Peltier module on the cold side was tested in appendix C to see if that would better balance the heat flow.

3.1.2 Heat Transferring Rods

The heat transferring rods are robust with a diameter of 21 mm and are fitted with removable aluminium caps that is in contact with the sample. Thermocouples are fitted along the rods to measure the temperature drop from the hot to the cold side of the measurement rig. The upper HTR is hollow, as seen in Fig. 3.1, so that gas is lead from the gas inlet to the sample. The thermal conductivity of the HTRs are an important parameter in calculating the heat transfer through them (see Eq. 2.4). Therefore, the heat transfer had to be verified in testing the rig on a material with known thermal conductivity (see subsection 4.2.3).

### 3.1.3 Compaction Pressure System

The lower part of the test rig is lifted by a pneumatic cylinder, pressing the HTRs together over the test sample. Air at a pressure of 10 bar is fed into an Aventics pressure regulator. This regulator uses a 24 V power supply and is controlled by LabView through a NI DAQ. The regulator acted instantly on the command signals from LabView. Rising and lowering the pressure, therefore, became a process over several steps, where the pressure changed only by small steps at a time. If not done this way, the pressure would change so fast that the sample would get pounded by the rapidly rising pressure. The measurement rig would also almost definitely be damaged by continuously being exposed to the shock the rapid pressure change would cause.

3.1.4 Insulation

To make sure the temperature measurements of the sample in the apparatus were not influenced by the external atmospheric conditions, a 3D printed insulation capsule was fastened around the sample and steel rods. The insulation capsule was made of a polylactic acid (PLA) material with low thermal conductivity. With a height of 18 cm, it covers approximately 85 % of the length of the steel rods. The outer diameter of the capsule is 8 cm. The PLA material has a melting point of 178 °C and its mechanical strength starts decreasing at 63 °C. During early testing, it was found that the insulation capsule had gaps where a small current of air could enter and influence the test. Especially because the test rig was placed inside a fume hood, air currents could cause problems. An improvement was made to the insulation capsule so that air currents were kept from reaching the sample and steel rods. The improvement was the including of cloth taped inside the gaps of the capsule and

to the top and bottom of it to close any opening. The improvements are visible in Fig. 3.3, where the open insulation capsule is depicted.
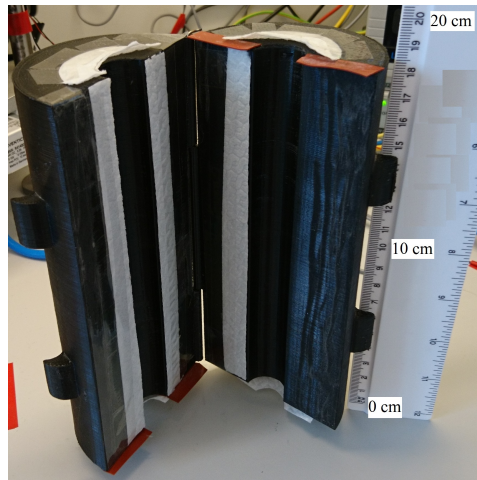
Figure 3.3: Insulation capsule for the test rig with visible padding for extra insulation.

3.1.5   Thermocouples

11 separate K-type thermocouples (nickel/nickel-chrome) are attached to the rig. 8 of them, visible in Fig. 3.1, are used to calculate the thermal resistance of the sample and the remaining 3 are used to measure the temperature of the Peltier modules and the room temperature. The thermocouples are connected to a NI thermocouple input module through two different panels and cables specialised for thermocouples. The thermocouple wires are fragile and demand careful handling. As they are fastened in the area where the sample is accessed, some contact was inevitable. A damaged thermocouple could be the source of great result errors. However, a damaged thermocouple or thermocouple wire gave such a temperature peak in its measurements that any damages were discovered at once and fixed.

3.1.6   Micrometers

The micrometers used to measure the thickness of the sample is of the type: Digimatic Indicator ID-S112XB, from Mitotoyo. They are placed as seen in Figs. 3.1 and 3.2 so that the mean measured thickness amounts to the thickness of the sample. There should have been three micrometers to make sure the sample was pressed together equally over the whole area. However, with three micrometers, the changing of the sample and removing of the insulation capsule would become almost impossible. Also pressure testing reveals an even force distribution over the sample (see subsection 4.2.2). The thickness of the sample is measured by subtracting the absolute measured value measured with a sample in the rig from the absolute measured value measured without a sample in the rig.

3.2 Gas Feed

A gas feed system was built for the rig so that tests could be carried out for gas saturated materials. Hydrogen and argon was to be used in this thesis. As hydrogen is a highly flammable gas, a purification system had to be included. Nitrogen gas was used to purify the gas feed system after each test with hydrogen. A simple T-valve was used to change from the test gas and nitrogen (see Fig. 3.4) For controlling the volume flow of the gas, a Burkert 8711 mass flow controller (MFC) was used. The aim for the volume flow was for it to be as slow as possible but still steady. It was calibrated for hydrogen with a max flow of 50 ml min^{-1}, but was tested to deliver a reliable gas flow as low as 1.0 ml min^{-1}. The volume flow test was done by holding the gas tube end under water and trapping the gas bubbles in a container with a known volume. As the MFC was calibrated for hydrogen and hydrogen and argon have quite different properties, the bubble test had to be carried out for argon as well. The argon gas showed a reliable flow like that of the hydrogen in the test.
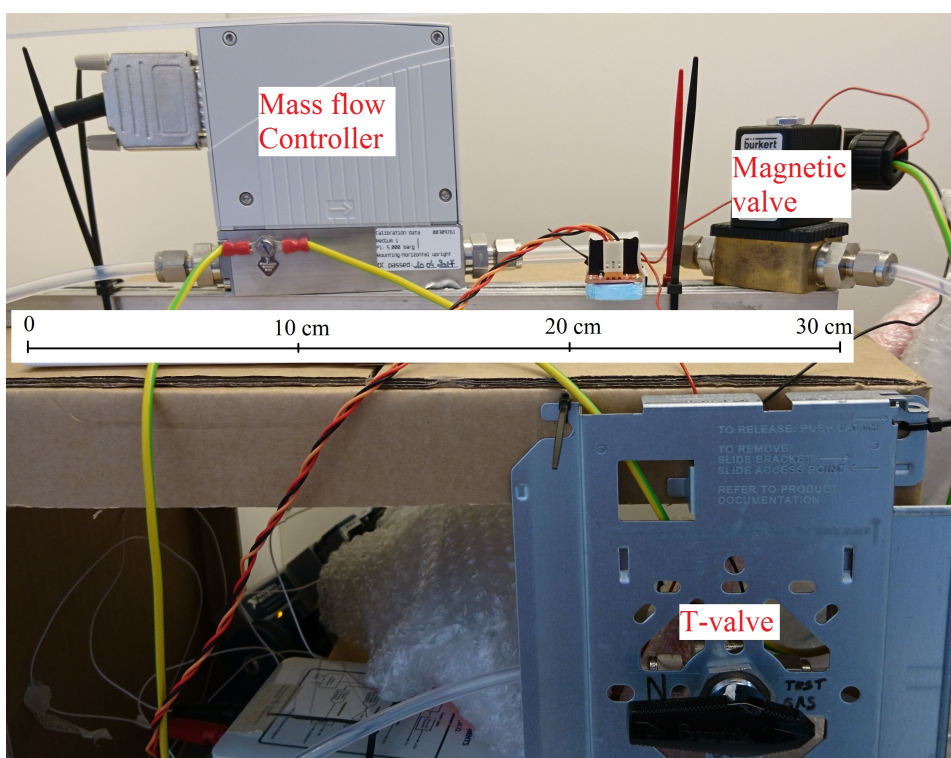
Figure 3.4: The gas feed system used to provide the gas for the gas saturated sample tests.

In addition to the MFC, a magnetic valve (MV) was installed as a safety measure. The MV is only open when exposed to a precise voltage signal. In that way, a power cut or another power related accident would cut the gas feed. This was important as fire or sparks was considered the biggest safety issue of the experiment. A water heating system was tested

to see if it was possible to control the temperature of the gas fed to the test rig, but that was found difficult. If the gas flow was to be kept as slow as possible, the time the gas used to travel from the heating system to the test rig was long enough to cool down the gas to room temperature. This was found to not be a problem as the testing was to be carried out at room temperature and because the slow flowing gas would be heated inside the upper stainless steel rod on its way to the sample anyway (see Fig. 3.1).

It was theorised after some testing with nonconclusive results that the gas entering the sample did not saturate the sample but in fact leaked away to one side or at least did not displace all the air in the sample. To overcome this problem, a hood was made to fit around the sample as seen in Fig. 3.5. For testing with hydrogen, the hood was sealed to the top rod so that the lighter hydrogen gas would displace the air. For argon, it was the other way around because of argon being heavier than air. After the fitting of this hood, the test results were more consistent.
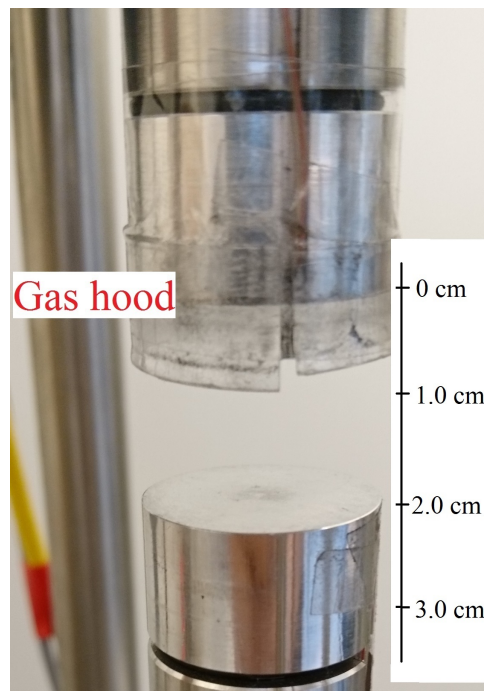
Figure 3.5: The gas hood fastened to the stainless steel rods to ensure a fully saturated sample.

To be sure the gas flow would not affect the thermal conductivity with forced convection in the sample, a couple of parameters was established. Firstly, the change rate of the control gas volume and secondly, the velocity of the gas when entering the sample. High velocity gas could also damage the sample physically. The diameter of the opening where the gas enters the sample is 1.0 mm. When the volume flow was kept at 1.0 ml min^{-1}, this would add up to a velocity of 0.021 m s^{-1}. This velocity was decided to slow to damage the sample. The change rate of the gas volume in the sample changes as the thickness of the sample changes. The smallest control volume measured is when only one sample of thin carbon paper is tested. The thickness of one carbon paper varies, but can be estimated to around 110 μm. This would make the control volume 0.030 ml in a 80 % porous material and the maximum change rate 0.56 s^{-1}. This was volume change rate was not considered large enough to create forced convection.

Chapter 4

Experimental

The experimental part of the thesis is explained in detail in this chapter. Both the approach for the main experiment producing publishable results and for side experiments carried out to ensure the reliability of the measurement rig.

4.1 LabView

LabView was used to control, give input and receive data from the measurement rig while testing. Only the physical adding and removal of the test sample could not be carried out by LabView. It provided temperature and micrometer measurements in log files used for further calculations. The block diagram for the final VI can be found in appendix A.

4.1.1 Front Panel

The front panel is the user interface in LabView. It has displays, buttons, and command windows used to control the rig while real-time information is visible. The left part of the front panel is fixed to the front panel. Displayed there is the most important information for the test. A screenshot of that part is found in Fig. 4.1. It is designed to look like the measurement rig so that the information shown is intuitive to read. The temperatures provided by the different thermocouples are listed in geometrical order in the stainless-steel rods and the micrometer values are displayed inside what looks like the micrometers. In addition, the name of the log file for the ongoing test, the pressure on the sample, the heat flow over and under the sample, and the deviation between the heat flows are shown. A green frame light up around the indicator showing the heat flows when the deviation between the is lower than the maximum value wanted for the test. This means that the test is progressing.

35
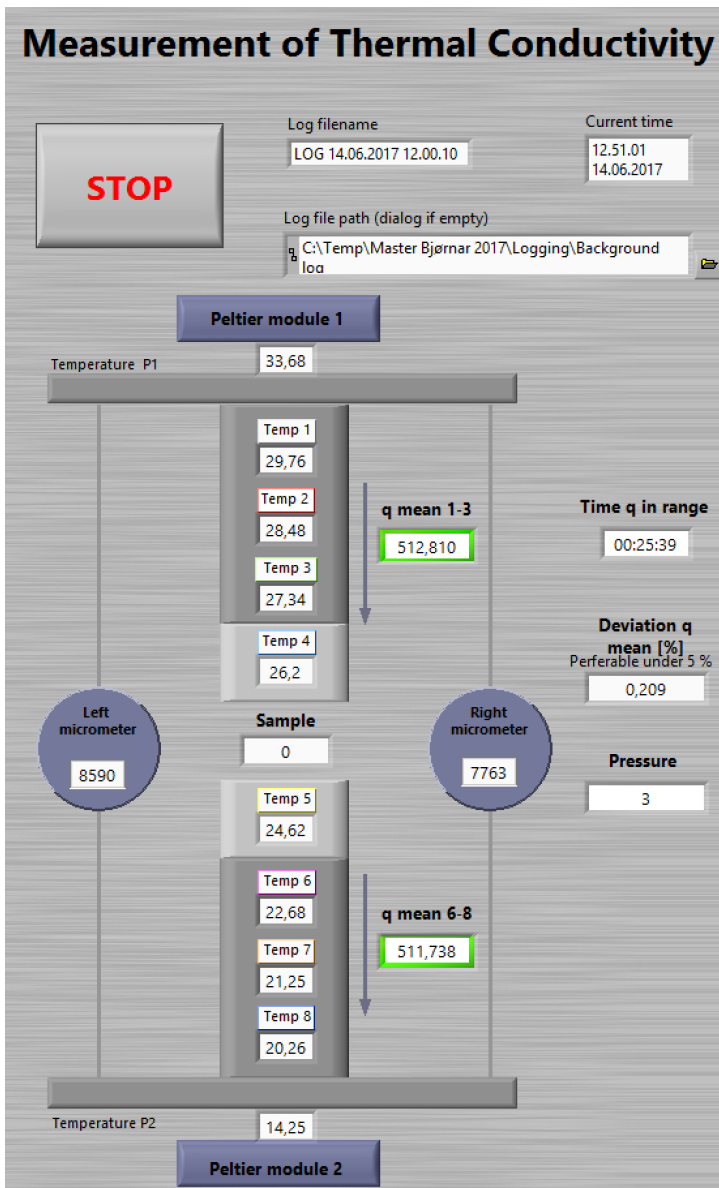
Figure 4.1: The fixed part of the user interface in LabView providing the most crucial information from the ongoing test.

The right side of the front panel is a tab window where it is possible to switch between different tabs that provide more information and control panels about different parts of the experiment. The first tab is the "Temperature" tab. This tab consists of three charts as seen in Fig. 4.2. The upper chart draws the real-time temperatures $T_1 - T_8$. T_1 relates to the top thermocouple in Fig. 3.1 and T_8 to the bottom one. By looking at this chart it is

possible to make out if something is interfering with any of the thermocouples as it then would act differently from the others. Steady state is visible in smooth lines in the chart. The middle chart display $\Delta T_{1-2} - \Delta T_{7-8}$, where $\Delta T_{1-2} = T_1 - T_2$. These should all be positive as the temperature decrease constantly from T_1 to T_8. The lower chart display the heat flows $\dot{q}_{1-3}$ and $\dot{q}_{6-8}$. These flows must be comparable to each other to predict the heat flow through the sample. Therefore, this is a chart that is paid close attention to throughout the experiment. The heat flows are provided by the Peltier modules, and by looking at the chart it was possible to adjust the power to the Peltiers for an optimal heat flow.
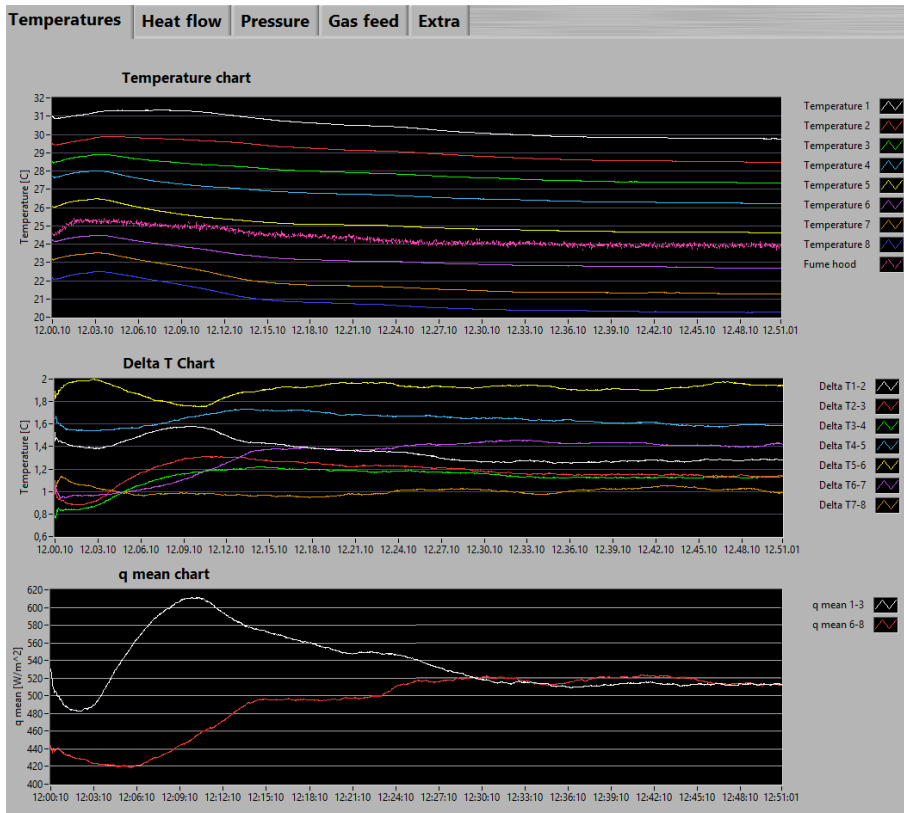
Figure 4.2: Temperature tab in the LabView front panel displaying temperatures and heat flows.

The test progress could be followed in the "Pressure" tab seen in Fig. 4.3. Displayed there are the pressures set to affect the sample during testing, and the time those pressures shall affect the sample at steady state before proceeding to the next pressure. When a wanted pressure is reached the indicator for that pressure lights up bright green. This made it easy to spot at a glance how far into the experiment one had come and when it would be completed.
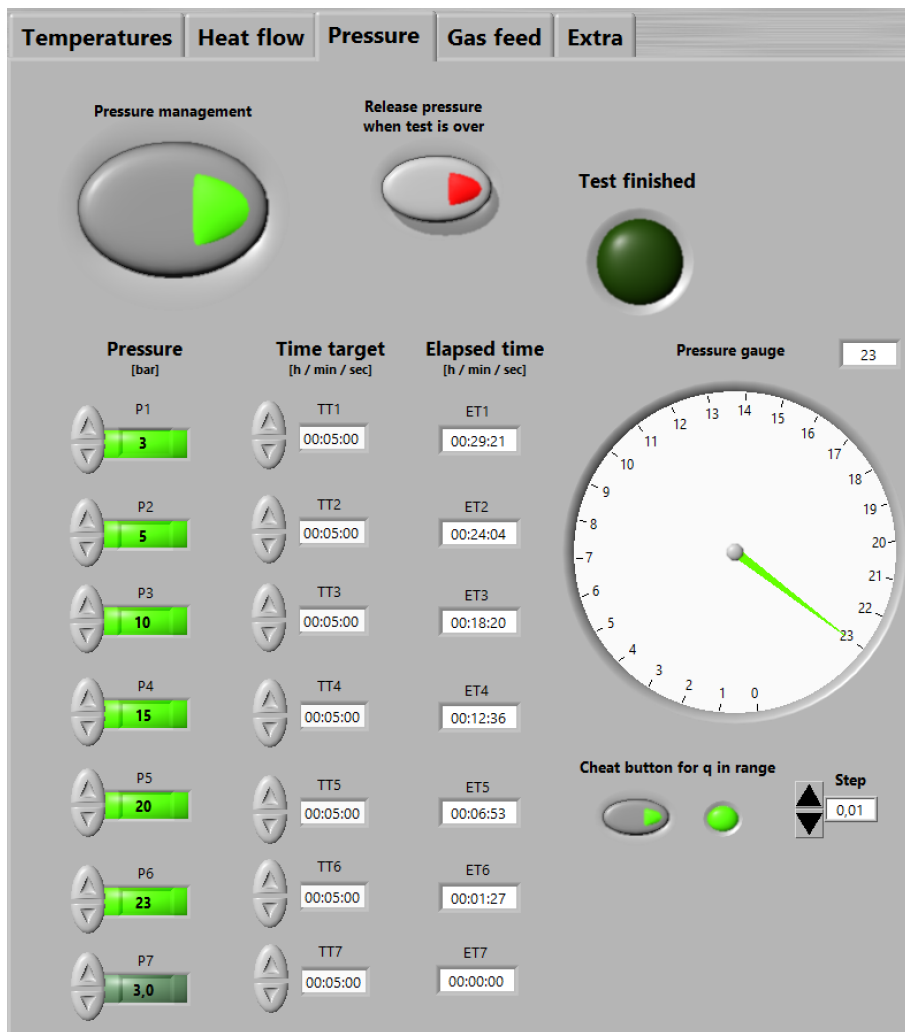
Figure 4.3: The Pressure management tab displayed the progress of the experiment with an overview of the pressures chosen for the test and the time that was to be used on each pressure.

When the sample was to be saturated with gas, that was controlled in the "Gas feed" tab seen in Fig. 4.4. Buttons was activated for what gas was to saturate the sample. Indicators and charts give an overview of the gas flow. A large button was used as an emergency switch. By pushing that button a magnetic valve closed off the gas feed immediately to prevent any further danger hydrogen or argon could cause. The hydrogen especially was considered a safety risk because of its high flammability. The two remaining tabs were the "Heat flow" tab where the maximum deviation for the heat flow was controlled, and the "Extra" tab was where all temperatures was listed so one could inspect in detail the numeric values displayed in the "Temperature" tab charts.
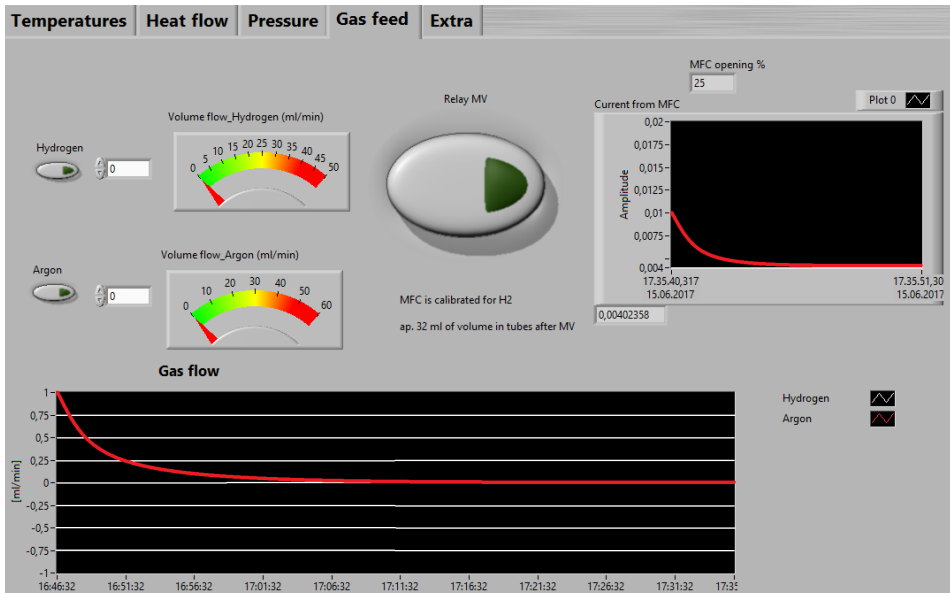
Figure 4.4: LabView front panel tab where the gas feed is controlled.

4.1.2 LabView code

The coding, that is done graphically with a block diagram, is set up in two while loops. A while loop is a is a part of the code that starts over when it reaches its end until certain requirements are met. In this case those requirements would be the stop button being activated. This means that the while loop is running over and over throughout the entire experiment. A tick count was put in to control the timing of the while loop. Measurements are being made one time per completed run of the while loop. Some processes demand more coding than others. Some of the more comprehensive processes were made in another window as an own VI and used in the main VI as a subVI block with input and output channels. The use of subVIs made the coding easier and more intuitive to read.

The lower window in Fig. 4.2 display the heat flow values used to see if the heat flow is constant through the steel rods and sample. These values are calculated continually once every while loop run in the coding using Eq. 2.4. The LabView block diagram code can be found in appendix A.

4.2 Calibrating the Measurement Rig

There are aspects of the measurement rig that could cause uncertainties connected with the measurements. Therefore, calibrations and testing was carried out to ensure the validity of any results from the main experiment.

4.2.1 Termocouples

The thermocouples used to measure the temperatures in the experiment had to be calibrated to measure the exact absolute temperature. This was done when the rig was first set up.[5] To calculate the heat flows, however, only the difference in temperature between the thermocouples had to be correct. A systematic error would therefore be of no concern for the final result. Furthermore, the systematic error occurring in the measurements $T_1 - T_3$ could differ from the systematic error in $T_4 - T_5$ as well as that in $T_6 - T_8$. Looking into the calculations used to find the thermal conductivity, it was found that the calibrations could be dropped to simplify the LabView code and still achieve the same results. The manipulating of the thermocouple measurements was therefore excluded from the LabView coding (see appendix A).

After the first results was presented, it was found that some of the measured contact resistances were negative (see subsection 5.1.3). A calibration was made in the calculation of the results to ensure the zero point for T_4 and T_5 was the same. After that adjustment, the results were all as expected and deemed valid.

4.2.2 Pressure testing

The test sample is compressed between two HTRs. For the reported pressure to be accurate and the measurements valid, the force on the sample had to be evenly distributed. The importance of an evenly distributed force is no less when testing with a gas saturated sample, where the gas could choose a flow path through the part of the sample that experience less pressure. This would keep the gas from intruding into a part of the sample and the sample would not be entirely saturated. The distribution of the force was tested when the measurement was first mounted [5] with a pressure measuring film, where microcapsules, spread on the surface of the film, was made to burst at a given pressure. The result of the pressure test is depicted in Fig. 4.5. The figure show busted microcapsules over the entire contact area. The pressure seems to be higher around the edges of the test than in the middle, but microcapsules have also burst in the middle of the thin pressure paper. The distribution was found to be adequately uniform, because the samples tested in this thesis are compressible. No changes that could have affected the force distribution have been made to the rig after that test. Therefore, the test already performed is regarded valid still.
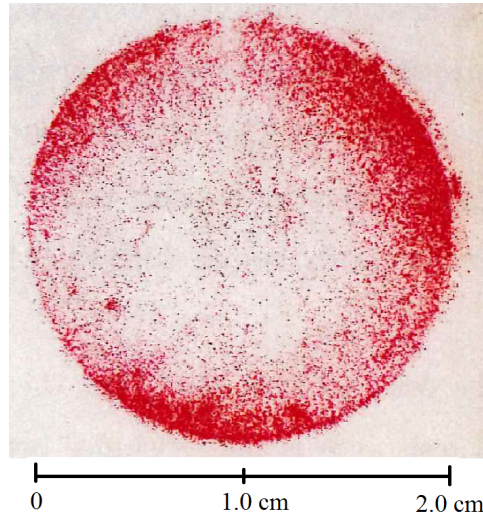
Figure 4.5: Result from the pressure film test. The pressure applied was 16.1 bar and seem uniform around the edges. This indicates that the HTRs are placed evenly onto each other.[5]

### 4.2.3 HTR Thermal Conductivity Calibration

To ensure the correct parameters for the thermal conductivity of the HTRs, κ_{ss}, the measurement procedure was tested for samples of a polyether ether ketone (PEEK) material with known thermal conductivity. the samples had been externally tested at the National Physical Laboratory in the UK and the PEEK material was found to have a thermal conductivity of 0.265 ± 0.020 W K^{-1} m^{-1}. This test had been carried out before for the rig, where κ_{ss} was found to be 10.3 ± 0.2 W K^{-1} m^{-1}.[5]. The same test was performed again and the earlier found value was considered valid still.

4.2.4 External influence

The main factor to be vary of during the testing was the influence of the atmospheric temperature distorting the temperature measurements by the thermocouples in the HTRs. Distorted temperature signals were a potential source of large errors. Because hydrogen saturated the sample in some of the tests, the measurement rig stood inside a fume hood to ensure the safety in the lab. This meant there would be a constant draft passing the rig. A screen was put up to avoid any direct draft on the rig, but the air circulation in the fume hood was still considerable. The screen is shown in Fig. 4.6. The insulation capsule protecting the HTRs and thermocouples from the environment was modified to not let any draft enter the thermocouples (see subsection 3.1.4). A fan directing the air flow through the cooling of the lower Peltier module was put into place, as seen in Fig. 4.7, to make the air flow and cooling more reliable and not so much influenced by the shifting turbulence of the uncontrolled fume hood air flow.
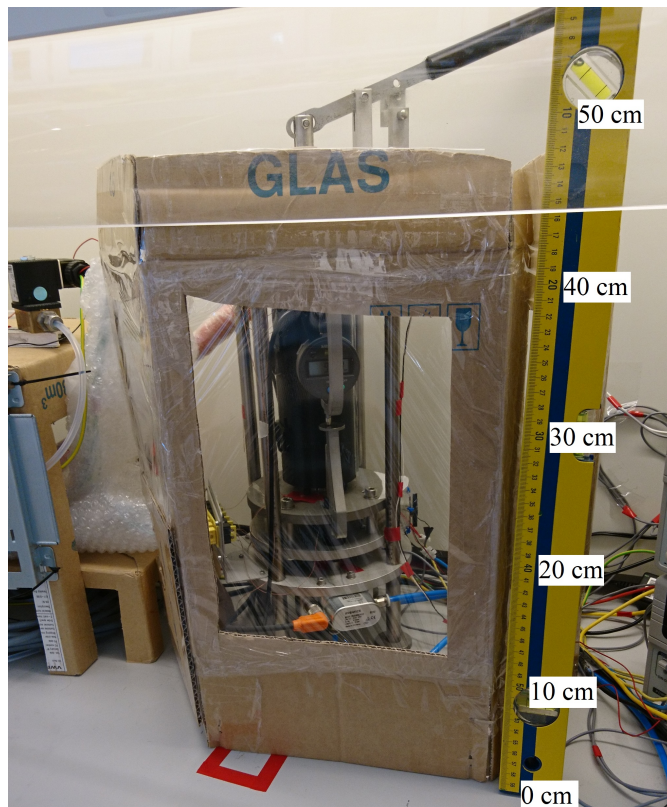
Figure 4.6: Screen protecting the test rig from the fume hood draft. Windows was cut in the screen and covered with plastic foil to ensure visibility.
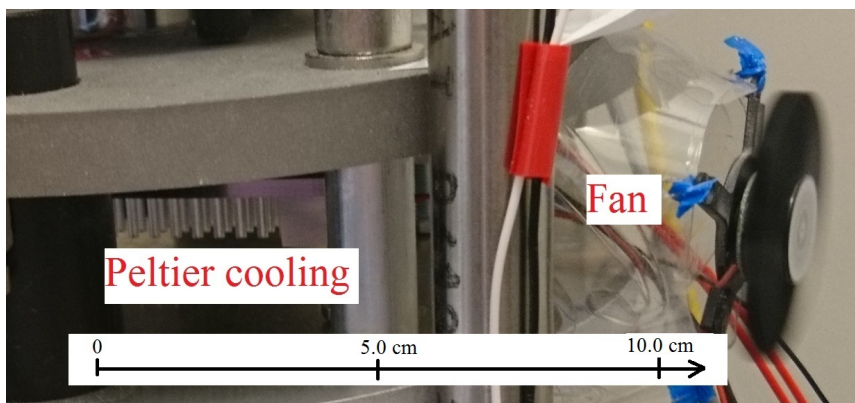
Figure 4.7: Fan added to the test rig to ensure a steady air flow through the cooling grid of the lower Peltier modules.

4.3 Measured Materials

The PTL materials tested in this thesis are the Freudenberg H1410 and Sigracet® 10BA. They have very different thicknesses. Where the measured thickness before testing was around 120 μm for the Freudenberg material, the measured thickness for the Sigracet® material was around 350 μm. The through-plane thermal conductivity should also be quite different.[39] An overview of the characteristics of the different PTLs are found in Tab. 4.1. The Sigracet® material is lighter than the Freudenberg material per volume because the Sigracet® material is almost three times as thick. This means the Sigracet® should be less compact and withstand compaction more poorly without deforming (see appendix D).

Table 4.1: Overview for tested PTL materials.[40, 41]

PTL material	Freudenberg H1410	Sigracet® 10BA
Mean thickness [μm]	120	350
Porosity [%]	-	88
PTFE treatment [wt%]	0	5
MPL layer [yes/no]	no	no
area weight [g m^{-2}]	65	85

4.4 Thermal conductivity of PEMFC components

Here follows an explanation of the proceedings of the measurements carried out in the laboratory where the measurement rig was used to find the thermal resistance of the GDL material.

4.4.1 Sample preparation

Circular samples of the PTL material measuring 21 mm were extracted from larger sheets of the materials using a hollow-punch tool. The samples was handled carefully and with gloves to avoid contaminating the samples. A pinch was used to touch the samples directly. Each sample's thickness was measured before they were tested in the rig. This was done to be able to measure the relative compression of the samples, as the lowest pressure for the rig is at 3 bar compaction pressure this had to be done outside of the rig. The thickness measurements were done with a highly accurate micrometer (Digimatic Micrometer from Mitotoyo Corporation). The samples were then arranged into stacks containing 1, 2, 3, and 4 samples to vary the thickness of the tested material. An overview of the relative compression of the samples/stacks tested can be found in Table D.

4.4.2 Testing Procedure

Before and after each sample test, the rig ran through all the compaction pressure stages once to calibrate the micrometers. This was done because the yield of the rig hardware had to enter the calculation when measuring the thickness of the sample. These calibrations lasted about 30 min, as there was no need to wait for the heat flow to stabilise before measuring the thickness values.

The circular sample or stack was carefully put on top of the lower HTR. It was important that the sample/stack was centred there so that the entire area was in contact with the HTR. If the test was to be carried out with gas entering the sample, the gas feed system had to start the gas feeding at this point. After upper HTR was lowered and the insulation capsule was fixed around the HTRs it was hard to be sure the gas entered the test. When using hydrogen, the gas detector described in appendix B was used to detect the gas flowing from the feed opening in the upper HTR. For argon, the gas feed was turned up far enough so that it was possible to see the gas flow by holding a paper cloth or something similar over the feed opening. The upper HTR was then lowered down onto the centre of the lower HTR and sample/stack.

After the sample/stack was fastened in-between by the HTRs in the lower position, the insulation capsule was fixed around the HTRs. Rubber bands or strips was used to close the capsule completely around the HTRs to make sure no drafts could enter. At this point, the compression of the sample/stack could begin. LabView was used for the pressure management and so by clicking the "pressure management" button the pressure slowly started increasing. A pneumatic plunger lifts the lower part of the measurement rig into a locking position. Even though the pressure increase at as slow pace, the measurement rig can seem to be held from moving because of the weight of the rig and friction between the lower part of the rig and the outer frame. Therefore, to avoid accumulation of pressure in the lower position to be released suddenly, the handle on top of the rig was used to manually help lifting the rig into its locking position. By doing this, a smooth transition was ensured. The manual helping started around 2.5 bar in LabView.

When the rig was locked in position, the compaction pressures was managed. How many stages there would be, what compaction pressures the stages would have, and how much time should elapse each stage should take was entered in the "Pressure management" tab. The time used on each step refers to the time for each step the heat flow through the sample must be stable before the system is deemed in steady state and measurements are made. The test proceed to the next compaction pressure step after the system is in stable state and the measurements have been made.

A wanted stability must be entered for the heat flow for the test to start, or only 0 % deviation will be accepted and steady state will be impossible to obtain. The normal time entered for each stage was from 20 min at the middle stages and 30 min at the first stage. The measurement rig is more unstable at the start of a test when it has just been opened and handled. Therefore, longer time is entered for the first stage to be on the safe side. For the last stage, only 5 min is necessary. That is because the last step happens after the maximum compaction pressure, when all temperature measurements are finished. The last step is only for measuring the thickness of the sample after the test to determine the permanent deformation of the sample/stack.

The test is over when a green led lamp in LabView, named "Test Finished", is activated. A button is bushed to release the compaction pressure, the gas feed system is locked down, and the LabView VI is stopped to save the background log. If necessary, nitrogen is used to rinse out the gas feed system. It could be risky to leave highly flammable hydrogen in the measurement rig. In the end, the sample/stack is removed and the test is run again without a test sample to calibrate the micrometers.

Chapter 5

Results and Discussion

Results are presented and analysed in this chapter. The results are plotted in figures to show graphically how the results change with pressure or thickness. Graphical software generated models, computed with the results from the thesis, are presented.

5.1 Measurement Results

Results produced through calculations with numbered equations are plotted in this section. The results are plotted in the order of how they are calculated. i.e. thermal resistance is used to calculate thermal conductivity, and is therefore presented first.

5.1.1 Thermal Resistance

Thermal resistance is found at for each stack by dividing the temperature drop over the stack by the area specific heat flow through it. By plotting r_{th} as a function of the thickness of the sample, the trend will be that r_{th} increase as the stack thickens. The slope of these plots indicates the thermal conductivity, as explained in Eq. 2.47. Figures 5.1-5.6 show six plots where the thermal resistance of the tested PTLs saturated with air, argon and hydrogen are presented as a function of sample thickness.
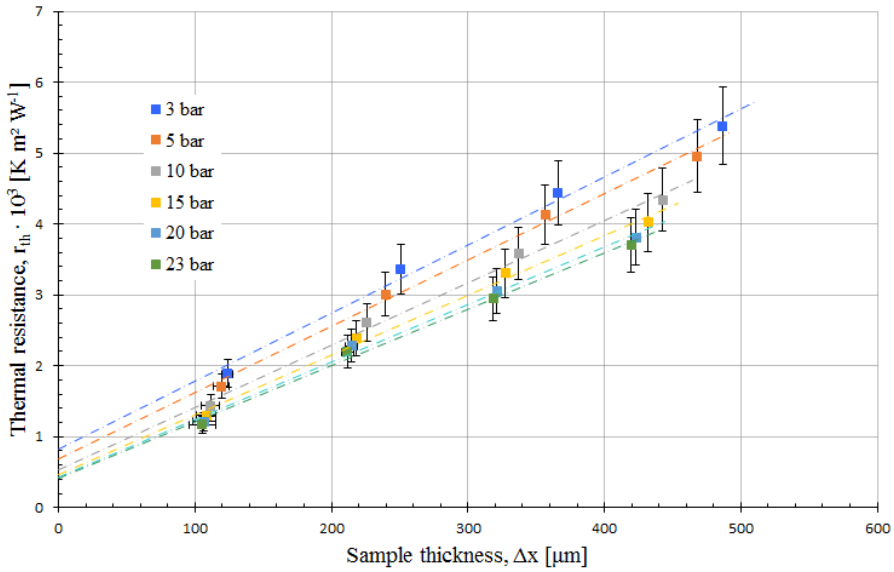
Figure 5.1: Thermal resistance for Freudenberg H1410 saturated with air plotted as a function of thickness. Each line represents a compaction pressure in the range 3 to 23 bar.
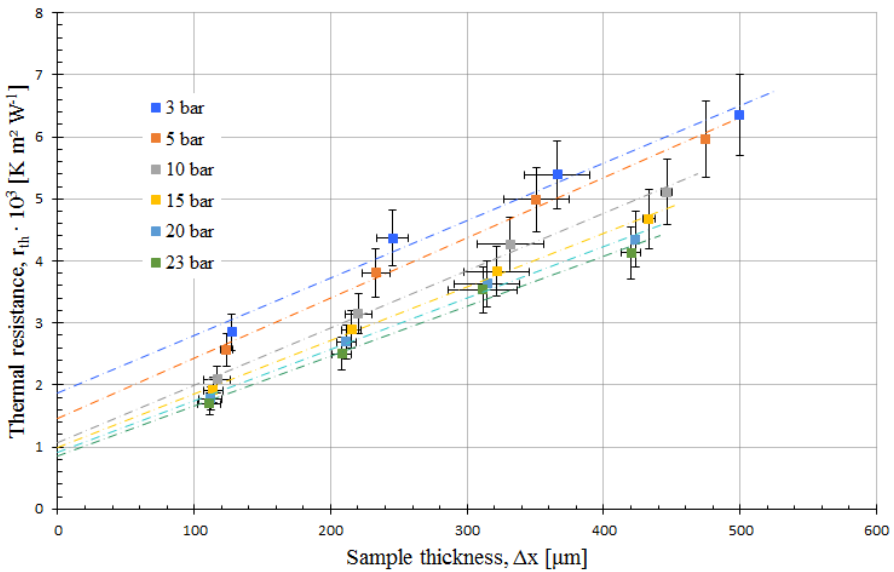
Figure 5.2: Thermal resistance for Freudenberg H1410 saturated with argon as a function of thickness. Each line represents a compaction pressure in the range 3 to 23 bar.
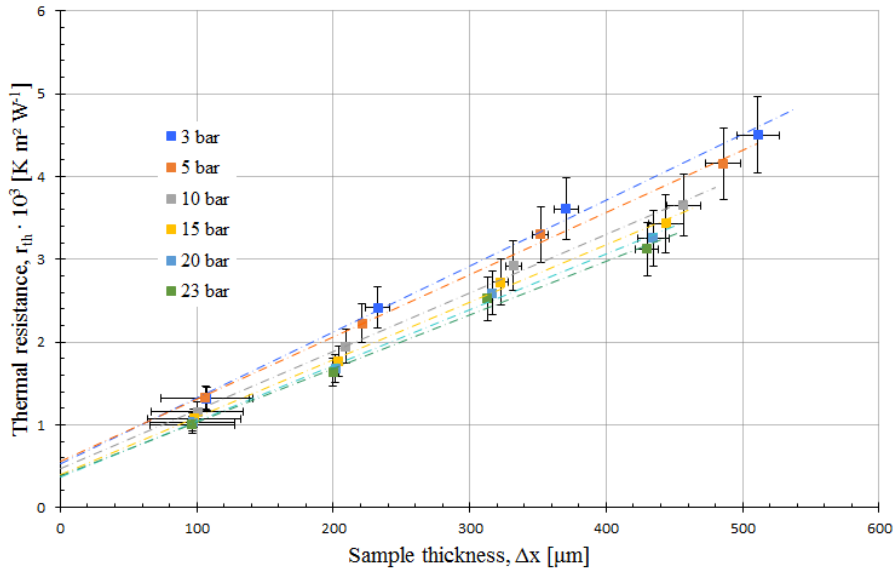
Figure 5.3: Thermal resistance for Freudenberg H1410 saturated with hydrogen as a function of thickness. Each line represents a compaction pressure in the range 3 to 23 bar.

Figure 5.4: Thermal resistance for Sigracet® 10BA saturated with air as a function of thickness. Each line represents a compaction pressure in the range 3 to 23 bar.

Figure 5.5: Thermal resistance for Sigracet® saturated with argon as a function of thickness. Each line represents a compaction pressure in the range 3 to 23 bar.
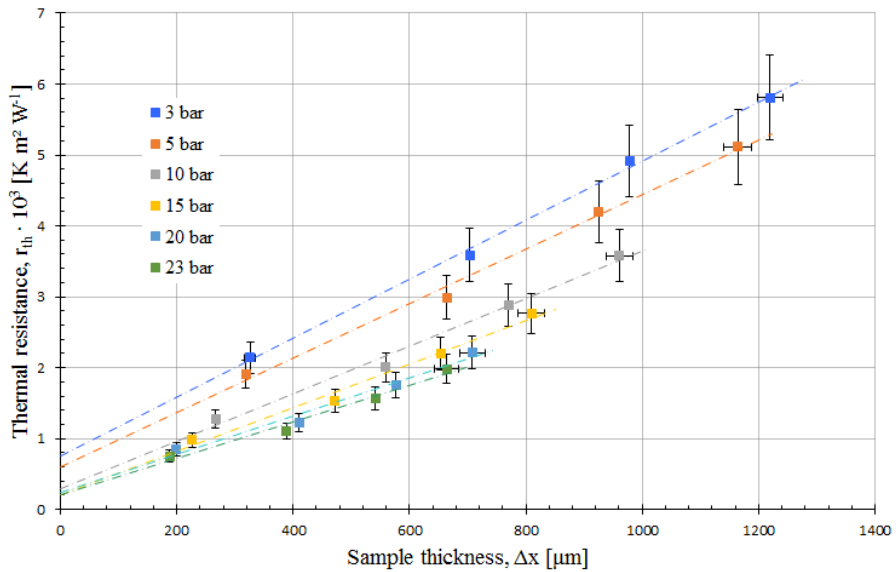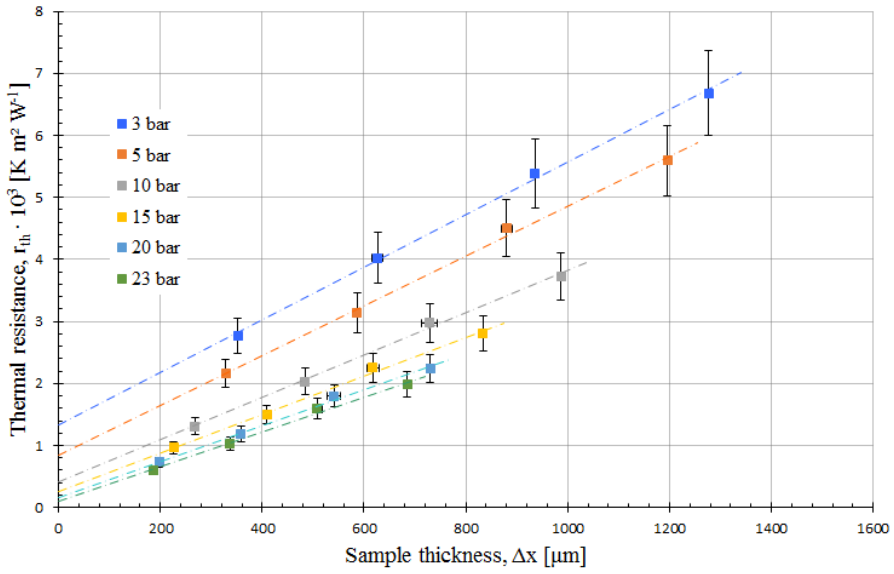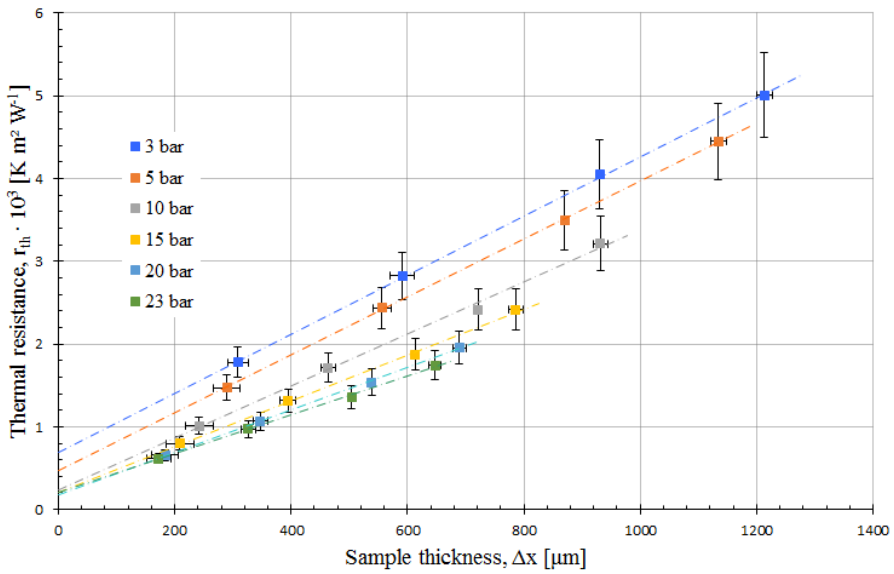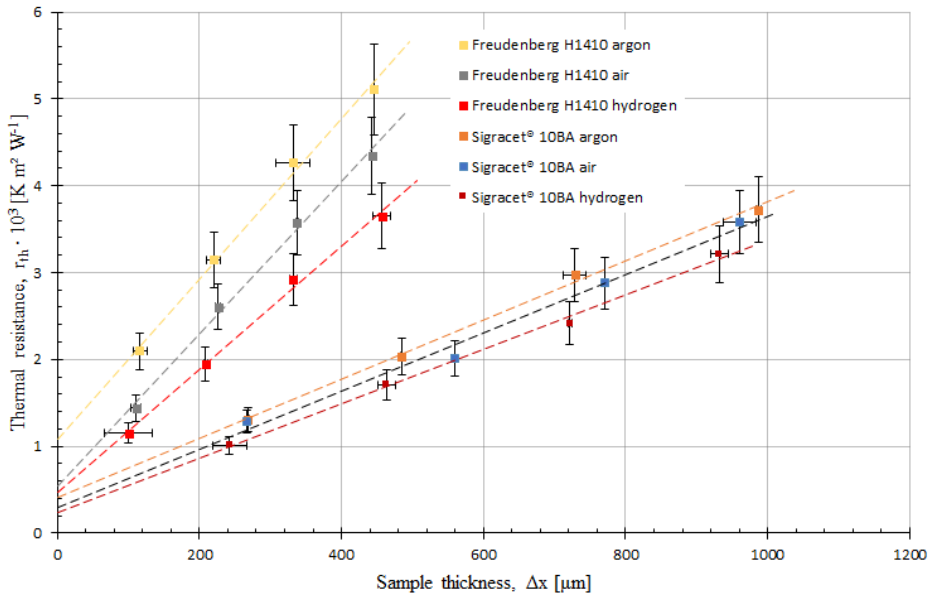

Figure 5.6: Thermal resistance for Sigracet® saturated with hydrogen as a function of thickness. Each line represents a compaction pressure in the range 3 to 23 bar.

All the plots in Figs. 5.1-5.6 have the same recognisable trend. The regression lines have a positive slope where the value of the slope increase with pressure. Also, the intercepting point at 0 bar is shown here. The intercept value is greater for the lower compaction pressures, which indicate that the thermal contact resistance is greater for lower compaction pressures. The fact that all the plots have all the regression lines lined up with the highest compaction pressure on the bottom and the others follow in order by size with dropping pressure, indicates that all the test were carried out without any major irregularities. Error bars are calculated from Eq. 2.37. The range of compaction pressure is from 3 to 23 bar due to the specifics of the pneumatic compaction tool.

Looking more closely on each of the plots, the regression lines have a higher slope for the Freudenberg H1410 PTL than for the Sigracet® 10BA. This indicates a higher κ value in the Sigracet® PTL than in the Freudenberg PTL. This is expected as the Sigracet® PTL materials has a higher thermal conductivity than Freudenberg PTL materials in general.[39] It is also possible to spot a difference for each of the gases. The argon gas in seem to give a higher slope and the hydrogen gas seems to give a flatter slope. The gas also seems to affect the intercept of the different regression lines, indicating an effect on the thermal contact resistance. Both the thermal conductivity and the thermal contact resistance are explored more deeply in new figures where they are plotted as new functions (see Figs. 5.8 and 5.9).

Inspecting Figs. 5.1-5.6 more closely, it is possible to spot the compression of the materials. The measurement points for each sample points to a lower Δx value for the higher compaction pressures than for the lower compaction pressures. The easiest way to spot this is by looking at the length of the regression lines. This difference is much clearer for the Sigracet® material than for the Freudenberg material. That is because the Sigracet® 10BA PTL is more compressible and yield more to the compaction pressure. The intercept points vary for the different test. In early results, some of the intercept points were negative. This was because of a systematic measurement error and is discussed more in subsection 5.1.3, Thermal Contact Resistance, as the thermal contact resistance is decided from the intercept point of the thermal contact resistance plot.

To better see the difference between the thermal resistance of the different materials and gases, a new plot is presented in Fig. 5.7, where thermal resistance for all the tested materials are plotted as a function of the sample thickness at 10 bar. Thermal resistance at 10 bar is plotted here because it is a likely compaction pressure in a PEMFC and used in earlier models.[39] κ found at 10 bar is also later used in the COMSOL modelling. It is expected that any differences between the measurements will be more prominent when presented in the same plot.

Figure 5.7: Thermal resistance as a function of thickness at 10 bar for Sigracet® 10BA and Freudenberg H1410 PTLs saturated with air, argon, and hydrogen.

The slopes of each of the graphs are easily distinguished from each other when they are plotted in the same figure, as in Fig. 5.7, where r_{th} is plotted for all tests at 10 bar as a function of sample thickness. The greatest difference is that of the different PTL materials, but also the gas present in the PTL makes a notable change in the results. Most notable for the results is that for both PTLs, even though very different in weight, compressibility, and thermal resistance, they are both affected the same way by the gas present. This is an expected result. Even though the thermal conductivities of the gases are lower than the thermal conductivities of the PTL materials, the high porosity of the PTLs makes the gases take up a large part of the volume and influence the total thermal resistance.

5.1.2 Thermal Conductivity

Thermal conductivity is the material constant normally used to calculate the heat transfer through a material. Therefore, the results presented in this subsection should prove most useful in further work regarding heat transfer in the PEMFC and any other application where gas is present in a porous material. Thermal conductivity is plotted as a function of compaction pressure in Fig. 5.8 for all materials and gases. It is expected that κ will increase with pressure for all tested materials.
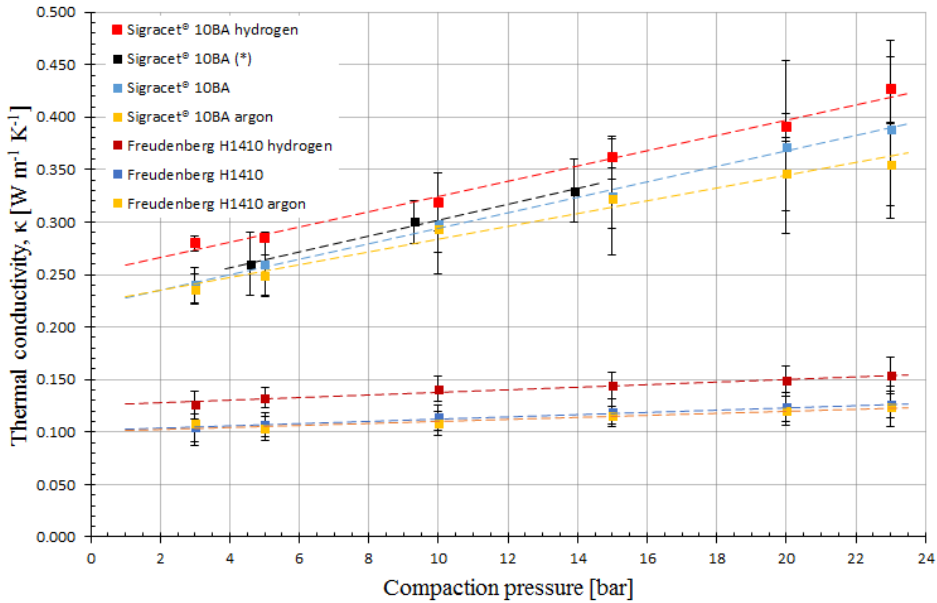
Figure 5.8: Thermal conductivity as a function of compaction pressure for Sigracet® 10BA and Freudenberg H1410 PTLs saturated with air, argon, and hydrogen. *External measurements.[39]

The thermal conductivity of the gas present in a PTL material clearly affect the total thermal conductivity of the PTL region. This is seen in Fig. 5.8. The measured thermal conductivity for Sigracet® 10BA saturated with air fits well with earlier measurements of the same material.[39] This is a strong indication that the measurement rig works properly and that the rest of the measured κ values are valid results.

As expected, the thermal conductivity is higher in a porous region if that region is saturated with a gas with higher thermal conductivity than the reference gas (air), and lower if it is the other way around. The difference between the air and hydrogen saturated PTLs are larger than the difference between the argon and air PTLs. That is expected as the difference in thermal conductivity is larger for hydrogen and air than for argon and air. This is particularly interesting for PEMFC materials where the anode side is completely saturated with hydrogen gas that has a thermal conductivity 7 times higher than air. i.e. thermal conductivity will be different in the anode GDL region from that in the cathode GDL region in a running PEMFC. Even though the exact same GDL material is used on both sides.

The results provided in Fig. 5.8 proves that the effect of the gas in the PTL is important to include in any future heat transfer calculations and models regarding PEMFC.

5.1.3 Thermal Contact Resistance

The thermal contact resistance is found by looking at the intercept point of the regression line in Figs. 5.1-5.6. It is small compared with the total thermal resistance. It is, however, interesting because it shows how the contact resistance change between an unyielding material and a compressible material at different compaction pressures.

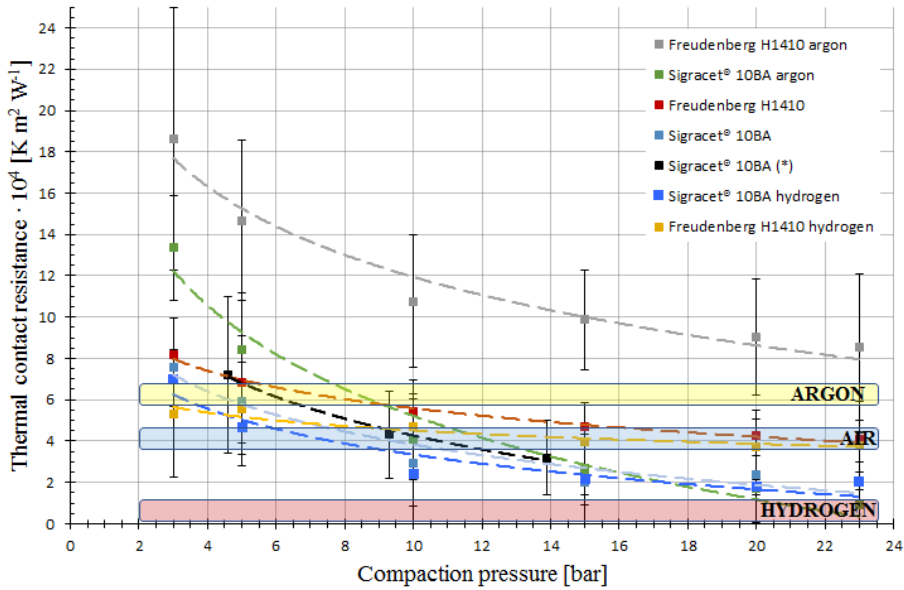**Figure 5.9:** Thermal contact resistance as a function of compaction pressure for Sigracet® 10BA and Freudenberg H1410 PTLs saturated with air, argon, and hydrogen. The colour boxes are the thermal resistances of 10 μm of the gases titled in the boxes. *External measurements.[39]

The decrease in thermal contact resistance with increasing pressure is clearly visible in Fig. 5.9. The reason for this is the change in number of contact points and total direct contact area between the carbon material in the PTL and the adjacent surface. Thermal contact resistance decrease for PTLs regardless of the gas it contains. However, the drop is greater for PTLs saturated with argon and smaller for PTLs saturated with hydrogen. This means that at low compaction pressures when the porosity of the PTL is greatest and the number of contact points between the PTL and its adjacent surface are limited, the thermal conductivity of the gas undoubtedly influence the thermal contact resistance. When the compaction pressure increase, a larger part of the surface is in direct contact with the carbon material in the PTL and the gas is displaced from the surface. Because of this, the thermal conductivity of the partly displaced gas will not influence the contact resistance as much for higher compaction pressures. The effect seems to be consistent regardless of what PTL material is used.

In early results some of the values were negative, something that would indicate that the thermal contact resistance would actually contribute to the heat transfer instead of resisting it. The thermal contact resistance progressed as expected relatively to the start at 3 bar for all values. However, the entire plot seemed to have shifted as if the zero value was wrongfully calibrated. Earlier results for the same material[39] gave another indication that all the measurements were systematically to small. See Fig. 5.10 for the results as they were before the calibration. The intercept values in some of the thermal resistance plots also became negative do to this error.
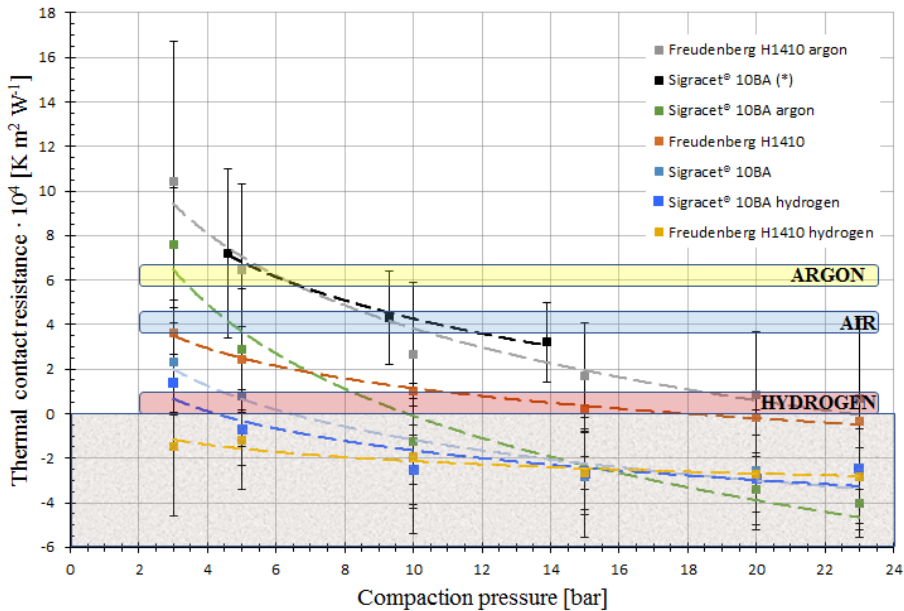

Figure 5.10: Thermal contact resistance as a function of compaction pressure for Sigracet® 10BA and Freudenberg H1410 PTLs saturated with air, argon, and hydrogen before calibrating the zero value of T_4 and T_5. The colour boxes are the thermal resistances of 10 μm of the gases titled in the boxes. *External measurements.[39] The area for negative thermal contact values is made grey to distinguish from the area for positive values.

As mentioned, the negative thermal contact resistance values were most likely the consequence of a wrongfully calibrated zero value. The first values that came to mind were the T_4 and T_5 measurements. The thermal resistance is calculated by dividing the temperature over the sample by the heat flow through the sample. ΔT_{4-5}, the temperature over the sample, directly affects the thermal resistance and is therefore a probable error source. The heat flow is calculated from a larger number of temperature measurements and is therefore less affected by a measurement error. Testing found that ΔT_{4-5} actually measured a negative temperature difference when there should be no difference at all. This difference was adjusted in the after treatment of the results. In further work, this calibration will be implemented into the LabView program.

After adjusting the ΔT_{4-5} value, there are no negative thermal contact resistance values in Fig. 5.9. As the error was systematic, the difference in the thermal conductivity made by the adjustment was negligible. The plot looks more like expected and the Sigracet® 10BA measurements match with earlier measurements of the same material. Also notable in that plot, is how the different measurements for the Sigracet® 10BA correspond to the thermal resistance of 10 μm of each of the gases used to represent the thermal contact resistance in the following COMSOL modelling (see section 5.2). The Sigracet® 10BA PTL saturated with air touch into the air box and the Sigracet® 10BA PTL saturated with argon touch into the argon box at around 10 bar, the chosen pressure for the COMSOL modelling. The rest of the measurements does not correspond as well to the gas boxes, but they are not far away.

5.2 COMSOL modelling

In this thesis COMSOL Multiphysics® is used to model the heat flow inside the PEMFC. The heat is produced near the middle of the MEA close to the membrane, as explained in subsection 2.4. The produced heat must be led from the PEMFC to avoid overheating the membrane and ensuring the efficiency of the PEMFC. The geometry of the modelled part of the MEA is shown in Fig. 5.11 and recognised from Fig. 2.4. Sections used for 1D modelling is coloured out in Fig. 5.11. These sections are especially interesting to model because as they represent the borders of the area and therefore will reveal the extremes of the model. The Temperatures along the membrane are interesting to model to be sure the membrane is not in any danger of scorching. From Fig. 2.4, where the modelling area is shown as a section of the larger PEMFC, the modelling area is symmetrically cut from the PEMFC. This means that the area outside the model just repeats what is seen in the model.
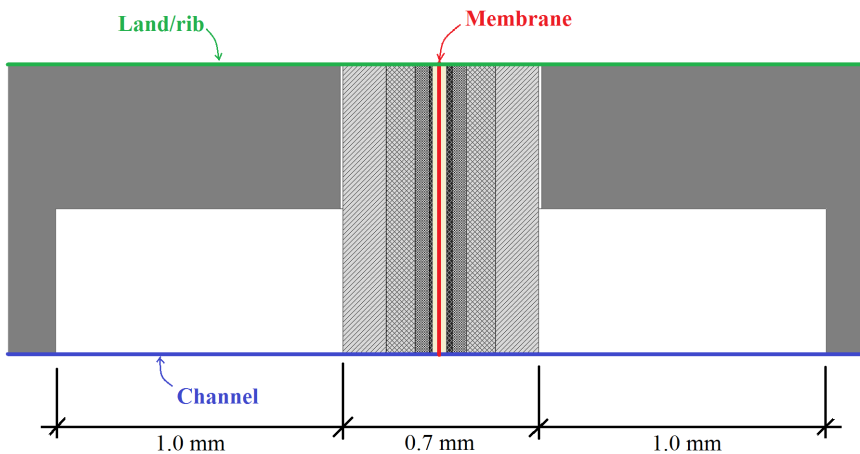
Figure 5.11: MEA geometry with coloured sections to show the base of the 1D models calculated in COMSOL.

When building the geometry of the part of the MEA that is interesting to model, all the different materials are given their own section. This is because the different materials are given individual properties. e.g. the thermal conductivity of the PTL differs from that in the MPL. Earlier thermal models of the MEA have been carried out without the consideration of the fuel gases in the GDL. This means that those models could be somewhat misleading depending on the effect the fuel gases have on the thermal conductivity of the GDL. COMSOL use Eq. 5.1 to calculate the models presented in Figs. 5.12-5.20. The equation considers that κ can change depending on the direction of the heat flow.

$$\nabla \left(\kappa_i \nabla T \right) + \dot{Q}_i = 0 \tag{5.1}$$

The heat sources used in the COMSOL calculations are shown in Tab. 5.1 and the thermal conductivities for the different calculated models are presented in Tab. 5.2. It is possible to see in Fig. 5.9 that the influence of the thermal conductivity of the gas in the PTL lessen as the material lose its porosity at greater compaction pressures, especially for compressible materials. As the thermal conductivity of the MPL-PTL interphase area has not been tested when saturated with gas, only an assumption can be made of how the gas affects it. Because of the density of the interphase area and the much greater thermal conductivity there, it can be assumed that the thermal conductivity of the gas will influence this area at a much smaller scale than in the PTL only area. The effect of the thermal conductivity of the gas is therefore assumed negligible and left out of the COMSOL model.

Table 5.1: Heat sources for COMSOL model.[4, 32]

Material	Heat source, q [W m^{-2}]
Anode	$0.001j + \frac{T\Delta S}{zF}j \cdot 0.80$
Cathode	$\left(0.5 + 0.07 log\frac{j}{10^4}\right)j + \frac{T\Delta S}{zF}j \cdot 0.2$
Membrane	$\frac{\Delta x_i}{8.7}j^2$
$j = 10\,000$ A m^{-2}	$E_{cell} = 0.67$ V

The through-plane and in-plane thermal conductivities differ much in PTL materials. In-plane thermal conductivities are assumed 10 times greater there than that found for through-plane in the results.[11, 12] Both properties are listed in Tab. 5.2 as they are separated in COMSOL. All thermal conductivity values for PTLs listed in Tab. 5.2, are values at 10 bar compaction pressure. Compaction pressure varies in the MEA from higher compaction pressure under the rip/land and lower compaction pressure in the gas channel of the bipolar plate. This small difference in compaction pressure is assumed close to negligible and not accounted for in the model, making the compaction pressure uniform.

Table 5.2: Thermal conductivities used in COMSOL model. In-plane κ values have been set to 10 times the value of through- plane κ in PTLs.[11, 12] *values measured in this thesis.

Material	κ (though-plane) [W m^{-1} K^{-1}]	κ (in-plane) [W m^{-1} K^{-1}]	Δx [μm]	ref.
Bipolar plates	20	20		[42]
Channel gas:				
Air	0.024	0.024	1000	[19]
Argon	0.016	0.016	1000	[19]
Hydrogen	0.168	0.0168	1000	[19]
PTLs:				
Freudenberg H1410				
Air saturated	0.114	1.14	150	[*]
Argon saturated	0.108	1.08	150	[*]
Hydrogen saturated	0.141	1.41	150	[*]
Sigracet® 10BA				
Air saturated	0.299	2.99	150	[*]
Argon saturated	0.293	2.93	150	[*]
Hydrogen saturated	0.319	3.19	150	[*]
MPL-PTL integration	15	15	100	[16]
MPL	0.18	0.18	50	[43]
Anode CL	0.18	0.18	10	[15]
Cathode CL	0.18	0.18	20	[15]
Membrane	0.25	0.25	50	[6]

Table 5.3: Substitute thermal contact resistances between the PTL and bipolar plates used in COMSOL model.[19]

Gas present in PTL	κ [W m^{-1} K^{-1}]	Δx [μm]	Resulting $r_{contact} \cdot 10^4$ [m^2 K W^{-1}]
Air	0.024	10	4.2
Argon	0.016	10	6.3
Hydrogen	0.168	10	0.60

In the scenario modelled in COMSOL, the MPL-PTL interphase region is included. It is expected that any effect from the thermal conductivity of the gas will be greater in a model where the PTL only region compose a larger part of the MEA.

The land 1D plots in Figs. 5.13 and 5.12 illustrate the temperatures through the MEA in a straight line where the bipolar plates are in contact with the GDL (see Fig. 5.11). Boundaries between two different materials are represented by dotted vertical lines in the plot. The figures show the difference in the temperature profile when hydrogen, air, or argon is present at the in the channel and in the PTL on the anode side. Figure 5.13 show the results for Sigracet® 10BA PTL and Fig. 5.12 show the results for Freudenberg H1410.
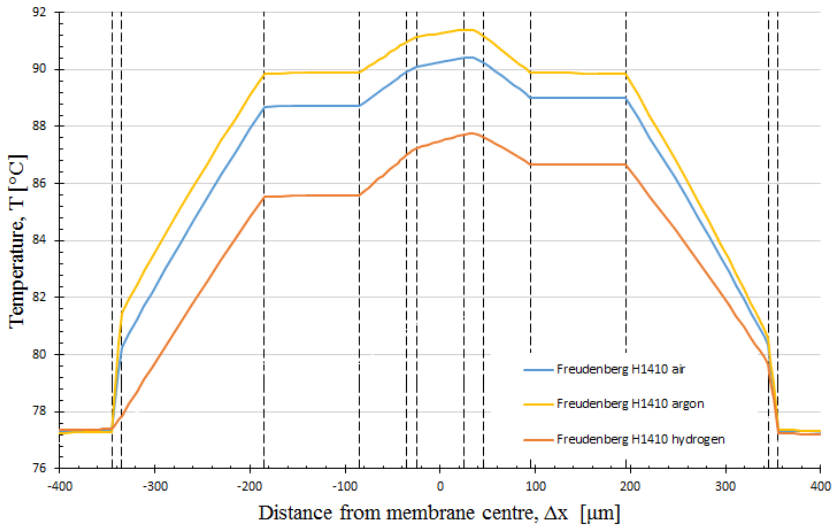
Figure 5.12: PEMFC land temperature profile with Freudenberg H1410 PTL saturated with air, argon, or hydrogen on the anode side. The dotted vertical lines represent the border between different materials in the MEA.
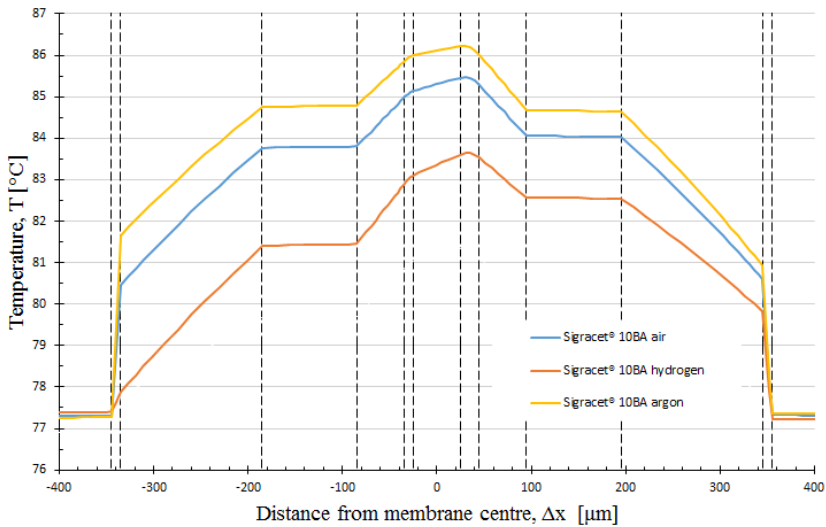
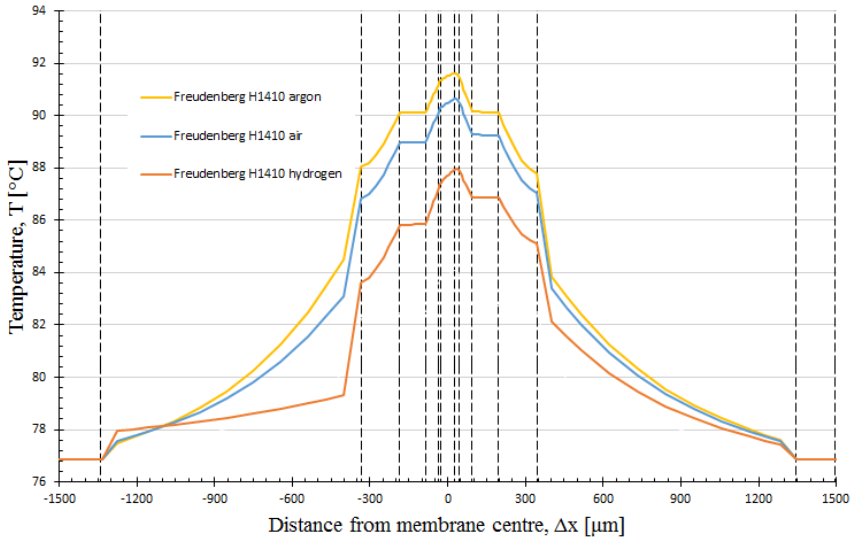
Figure 5.13: PEMFC land temperature profile with Sigracet® 10BA PTL saturated with air, argon, or hydrogen on the anode side. The dotted vertical lines represent the border between different materials in the MEA.

In Fig. 5.12, the temperature profile through the land of the MEA is shown for a Freudenberg H1410 PTL saturated with air, argon, and hydrogen. It is easy to see that the heat in the MEA is mostly produced in the boundary region between the catalyst layers and the membrane. As expected, the hydrogen saturated PTL transports heat away from the centre of the MEA better than the PTL with air or argon.

The largest temperature drop difference between the different cases is in the boundary region between the bipolar plate and the PTL. The 10 μm gas gap influence the total temperature drop considerably. With argon in the PTL, the temperature drop from the hottest point to the outer boundary is approximately 14 °C, for the case with air in the PTL, the temperature drop is just over 13 °C, and for the case with hydrogen in the PTL, it is just under 11 °C. This means that the difference between the traditional model, where all PTLs use a κ found in air, and the case where there is hydrogen on the anode, as it is during operation, is over 2 °C. A temperature of 2 °C seem small, but it decreases the temperature drop with over 15 %. That amounts to a considerable difference in transported heat from the centre of the PEMFC (see Eq. 2.4).

The temperature profile through the land of the MEA for a Sigracet® 10BA PTL saturated with air, argon, and hydrogen is presented in Fig. 5.13. Also here the hydrogen saturated PTL transports heat away from the centre of the MEA better than the PTL with air or argon. The Sigracet® 10BA PTL have a higher thermal conductivity than the Freudenberg H1410 PTL. Therefore, the temperature drops, from the middle of the MEA to the outer boundary of the model, are smaller for all the cases with the Sigracet® PTL. With argon in the PTL, the temperature drop from the hottest point to the outer boundary is just over 9 °C, for the case with air in the PTL, the temperature drop is about 8.5 °C, and for the case with hydrogen in the PTL, it is about 6.5 °C. This gives a difference from the new to the traditional model of about 2 °C. The thermal conductivity is higher for the Sigracet® PTL and one would, therefore, that the κ of the gas would have less influence on the total thermal conductivity in the PTL region. However, porosity of the Sigracet® PTL is higher than that of the Freudenberg PTL, providing more volume for the gas to saturate.

The channel 1D plots illustrate the temperatures through the MEA in a straight line through the gas channel (see Fig. 5.11). Figure 5.15 show the results for the Sigacet® 10BA PTL and Fig. 5.14 show the results for the Freudenberg H1410 PTL. The influence of the gas present on the anode is expected to be larger in these plots. That is because conductivity of the gas in the channel will influence the results as well as the gas in the PLT material.

Figure 5.14: PEMFC channel temperature profile with Freudenberg H1410 PTL saturated with air, argon, or hydrogen. The dotted vertical lines represent the border between different materials in the MEA.
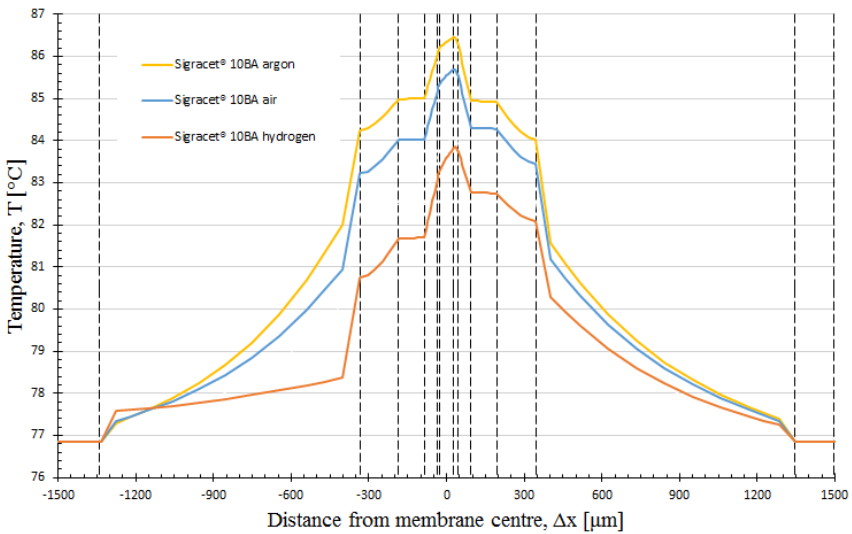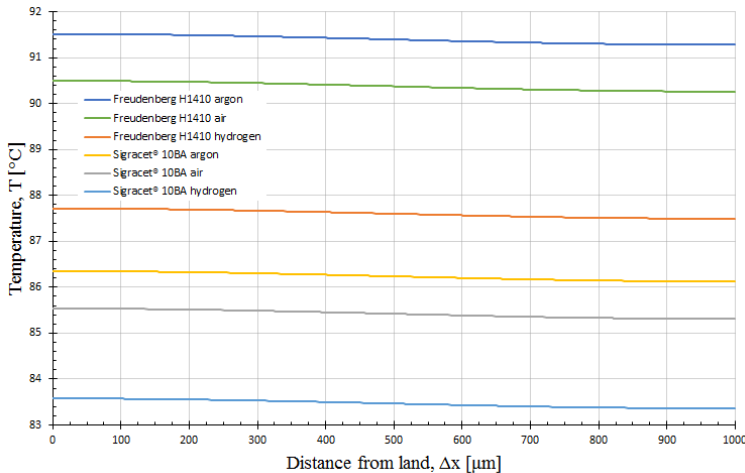

Figure 5.15: PEMFC channel temperature profile with Sigracet® 10BA PTL saturated with air, argon, or hydrogen. The dotted vertical lines represent the border between different materials in the MEA.

In Fig. 5.14, a large temperature drop can be spotted in the gas channel. This temperature drop is highly dependent on the thermal conductivity of the gas in the channel. Therefore, the drop is much larger for the argon and air than for the hydrogen. In the case with argon in the Freudenberg H1410 PTL, the temperature drop is almost 15 °C, when air is present, the drop is almost 14 °C, and when hydrogen is present, it is around 11 °C. A difference of almost 3 °C from the traditional to the new model amounts to a change of about 20 % in the temperature drop.

The different cases with the Sigacet® 10BA PTL is presented in Fig.5.15. The trend is similar to that of the previous model results. The higher thermal conductivity in the Sigacet® 10BA PTL makes the temperature drop from the centre of the MEA to the outer boundary of the model in those cases smaller than for the cases where Freudenberg is the PTL material. The temperature drop is about 9.5 °C in the argon case, 8.5 °C in the air case, and almost 7 °C in the hydrogen case. That gives a difference of 2.5 °C (over 25 %) from the traditional model.

The temperature in the membrane is crucial for the performance of the PEMFC. If the membrane is overheated it can scorch and become completely disabled from performing its tasks. The temperature seems higher in the middle of the channel when comparing the 1D plots for the channel and land. The case where the membrane is hottest is in the case where Freudenberg H1410 PTL is saturated with argon on the anode. Figure 5.16 shows the temperature profile from the channel to the land of the model as drawn in Fig. 5.11. The temperature difference in the membrane is not easily spotted, but at a close look, it is a bit warmer at the land than in the middle of the channel. This happen when the thermal conductivity is higher in the bipolar plate than it is in the gases in the channel.

Figure 5.16: Membrane 1D plot illustrating the temperature profile in the middle of a PEMFC membrane from the channel to the land, with Sigacet® 10BA and Freudenberg H1410 PTLs saturated with air, argon, and hydrogen on the anode side.

Comsol can also produce 2D plots so that it is possible to see the temperature profile in the entire modelled MEA region. When looking at the temperature profile of the entire model, it is easier to spot where the heat transfer is greatest. Two different plots are used to present the temperature profile. One shows the temperature with isotherms and the other with colour brightness. The Sigacet® 10BA PTL is used to present the difference in the 2D MEA temperature profile from air to hydrogen. Presented in Figs. 5.17 and 5.18 is the isotherm plot for the Sigacet® saturated with air and hydrogen on the anode side.
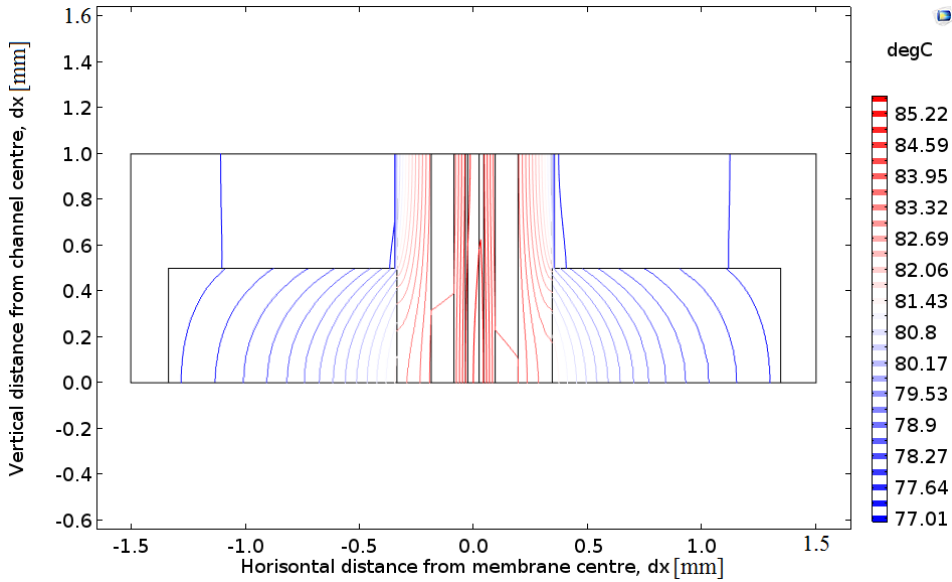
Figure 5.17: MEA region modelled in COMSOL showing the temperature drop through the different layers of the PEMFC using isotherms. Red isotherms represent higher temperatures than blue isotherms. The PTL is a Sigacet® 10BA saturated with air.
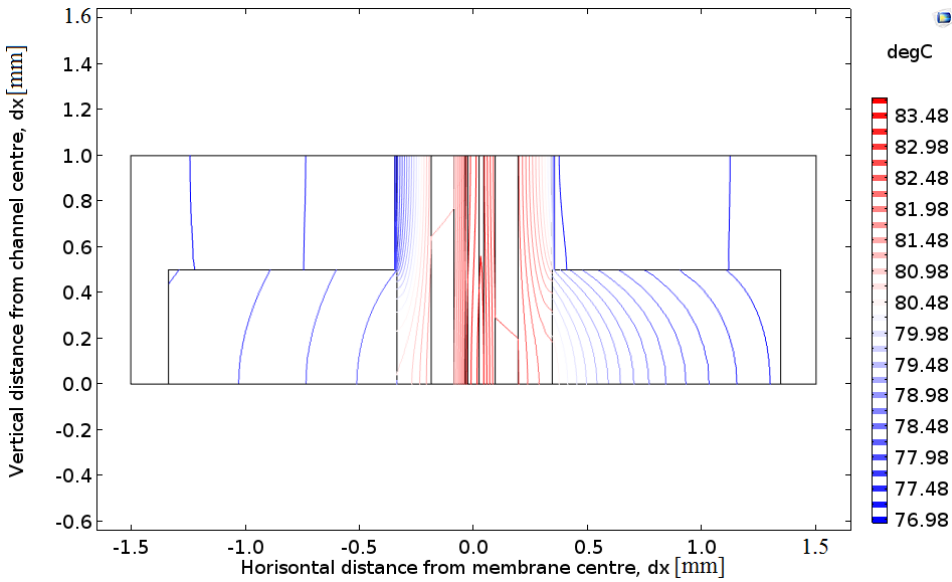
Figure 5.18: MEA region modelled in COMSOL showing the temperature drop through the different layers of the PEMFC using isotherms. Red isotherms represent higher than blue isotherms. The PTL is a Sigacet® 10BA saturated with hydrogen.

The most obvious change when comparing Figs. 5.17 and 5.18 is the difference between the almost symmetrical horizontal temperature distribution when the PTL is saturated with air and the unbalanced distribution when it is saturated with hydrogen. The anode side in the plot with the hydrogen saturated PTL seem to have a lower temperature than the air saturated cathode side. This, again, points to a more efficient heat transfer on the anode side.

Figures 5.19 and 5.20 plots the temperature drop through the MEA using colours brightness. The plot immediately points out where the heat is produced and where it is most efficiently transported away. The difference between the air and hydrogen saturated Sigacet® 10BA PTL, is used here as well to spot the most prominent differences between the traditional model and the model provided by this thesis.

Figure 5.19: MEA region modelled in COMSOL showing the temperature drop through the different layers of the PEMFC using colour brightness. A bright colour represents a higher temperature than a dark colour. The PTL is a Sigacet® 10BA saturated with air.

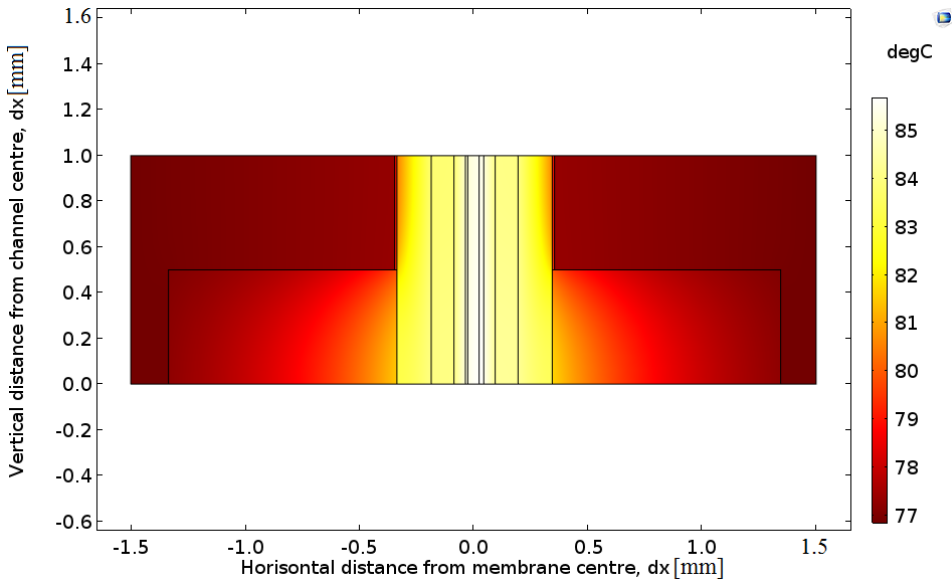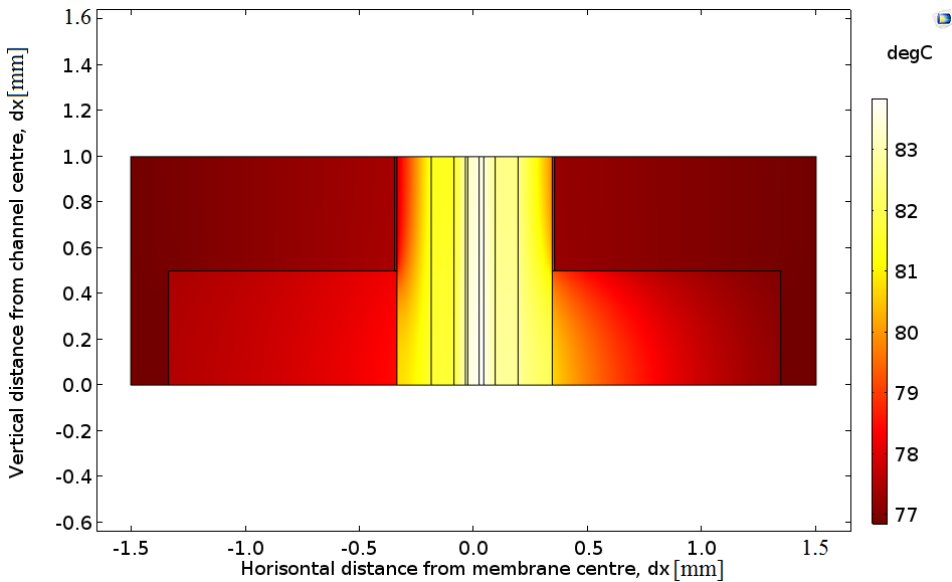**Figure 5.20:** MEA region modelled in COMSOL showing the temperature drop through the different layers of the PEMFC using colour brightness. A bright colour represents a higher temperature than a dark colour. The PTL is a Sigacet® 10BA saturated with hydrogen.

The difference between the symmetrical Fig. 5.19 and the slightly unbalanced colour brightness in Fig. 5.20, is not as easily spotted as in the isotherm plots. However, there is undoubtedly a difference as also here the temperature seems to be slightly lower on the anode side, hinting to a more efficient heat transfer from the centre of the MEA to the border of the COMSOL model on the hydrogen saturated anode side.

Chapter 6

Discussion Remarks

In this chapter, the acquired results are discussed by reflecting on how they, together with the analysis and COMSOL modelling, answer the issue raised by the thesis. Weaknesses in the measurement rig and other possible error sources are considered. Suggestions are given for improvement, if possible. In the end, a proposition is made for how further work should proceed.

6.1   Results

It was theorised that the thermal conductivity of a gas, present in a porous material region, would affect the total thermal conductivity of that region. the results point to validate this theory. Before the theory can be confirmed, all other reasons for the results changing the way they did for the different gases must be ruled out.

The thermal resistance in the PTL samples dropped when they were saturated with hydrogen as opposed to air. Thermal resistance is measured in the sample by dividing the temperature drop over the sample by the heat flowing through the sample. If the temperature of the entering gas deviates much from the temperature in the sample, that could affect the temperature drop measured over the sample. When measuring PTL materials saturated with air, there is no gas feed into the sample to affect the temperature measurements. For the temperature of the gas to make the results show a drop in thermal resistance, the temperature on top of the sample must be affected by a gas at a lower temperature than the sample or the temperature on the bottom side of the sample by a gas at a higher temperature than the sample. The temperature in the sample is kept as close to room temperature as possible. Therefore, and because of the long distance for the gas through tubes at room temperature, the sample and gas should be at roughly the same temperature.

The gas enters the rig near the top of the upper HTR (see Fig. 3.1). From there it runs through the upper HTR down into the sample. If the gas is at room temperature when reaching the gas inlet, the gas can be heated inside the hot upper HTR. This contradicts the possibility that cool gas could affect the temperature upper part of the sample, where the gas enters the sample, as the gas would more likely be heated than cooled before entering the sample. Also important, is the fact that the temperature drops gradually through the HTR. Therefore, if the gas was to be heated near the top of the upper HTR, the temperature in the gas would just as easily drop inside the HTR on the way down into the sample.

If the temperature of the gas cannot alter the temperature measured over the sample, the temperature of the gas would have to change the measured heat flow through the upper HTR. For the thermal resistance to drop the measured heat flow through the sample must increase. The heat flow through the sample is derived from the mean value of the heat flow in the upper and lower HTR. Therefore, an increase in heat flow in the upper HTR would cause an increase in heat flow through the sample. When the gas enters the inlet, it is cooler than the part of the HTR it enters, possibly contributing to cooling the upper part of the HTR. This would lower the temperature drop over the length of the HTR and contribute to lower the heat flow, not increase it. It can therefore be concluded that only the thermal conductivity of the gas affect the results and not the internal energy of the gas as it enters the sample. Also, the fact that thermal resistance increase in the argon saturated PTL proves that anything other than the thermal conductivity of the gas could not have contributed to affect the results from the tests.

Through-plane thermal resistance for PTLs are much greater than the in-plane thermal resistance. The reason for this is the direction of the fibres in the PTL and the resulting directional difference in contact points. A trend in the results demonstrating this argument, was shown when the thermal resistance of the material dropped each time the compaction pressure increased. The in-plane fibres broke or bent under higher compaction pressures to create more through-plane contact points. This trend was consistent regardless of the gas present in the PTL. However, the drop in thermal resistance and thermal contact resistance was more abrupt for the PTLs with argon present. This was because the argon gas had an insulating effect that was removed when the sample was compressed and the gas was displaced.

The permanent damage to the PTLs from the breaking of the fibres was greater in the lighter and more compressible Sigracet® 10BA PTL than in the more compact Freudenberg H1410 (see appendix D). An increase in through plane contact points was also proven by the thermal contact resistance results, where the thermal contact resistance dropped with increasing compaction pressure. This points to an increase in contact points between the PTL and the adjacent material as well as inside the sample itself with increasing compaction pressure. The logarithmic trend of the thermal contact resistance when plotted as a function of compaction pressure (see Fig. 5.9), points to the thermal contact resistance approaching zero at unlimited compaction pressure. This is a strong argument for the validity of the results.

Thermal conductivity of the PTLs changed as expected when they were saturated with different gases with different thermal conductivity. That can be seen in Fig. 5.8. The difference in thermal conductivity is greater between hydrogen and air than it is between argon and air, something clearly demonstrated by the small distance between the air and argon lines and the larger distance between the air and hydrogen lines. The measured thermal conductivity for the Sigracet$^®$ 10BA PTL fit well with earlier measurement of the same material, a strong indication that the results are valid. The thermal conductivity increased overall by 20 - 25 % in the Freudenberg H1410 PTL and 10 - 15 % in the Sigracet$^®$ 10BA PTL when saturating them with hydrogen. The reason the Freudenberg is affected more severely is that it has a thermal conductivity of about half of that in the Sigracet$^®$ and therefore also smaller relative to the thermal conductivity of the gas.

The COMSOL model results demonstrated a notable change in the temperature profile through the MEA due to the change in thermal conductivity of the materials in the model. The change was visible at the 1D plots of the membrane, land, and channel and in the 2D plots of the entire MEA region. This strongly suggests that an updated thermal conductivity value must be implemented in all future models and simulations regarding the temperature profile and transport of heat in the PEMFC to avoid producing misleading results.

6.2 Error Sources

For the results produced by the tests and calculations in this thesis to be trusted, all error sources had to be identified and inspected. The most probable source of error was the measurement rig and its LabView programming. The math used to calculate the results from the measurements is uncomplicated and any error connected with it would be discovered fast, as the calculated results would mismatch with the expected results from trends in the dataset provided by the test. To be safe, the math was brought up and discussed several times, especially because the after treatment and calculations of the measurements were in the process of being programmed into a software program to streamline the test process.

The measurements used to calculate the results were made by the thermocouples and micrometers in the test rig. The micrometers were calibrated between each test to make sure the zero value for the sample thickness measurements were valid even if the measurement rig yielded to the high compaction pressure. This constant calibrating was time consuming, but it was deemed the only way of ensuring the validity of the sample thickness measurements.

Eight thermocouples was used for the temperature measurements. They consist of fragile wires and cables that easily got in the way of the person operating the rig. At several occasions, the fragile part of a thermocouple broke because they were in the way of the person managing the rig. Luckily, the tiniest crack in one of the small wires made for a temperature measurement of - 2 000 °C. Because of the major deviation in case of an error, the error was discovered and fixed fast. Regardless, the test would be on hold because of the deviation in the heat flow. If any doubt should arise about the validity of the measured temperatures, a calibration would follow and the measured values would be adjusted in the LabView program.

The draft in the fume hood was a constant threat to the temperature measurements. The HTRs was insulated as well to avoid any draft influencing the measurements. A screen was also set up in front of the entire measurement rig. The turbulent air in the fume hood probably made it harder to stabilise the heat flow, but when the measurements were made, they were stable, and had been for a while. The LabView program made sure no measurements were made outside of steady state.

6.3   Future Work

In the future, the method used in this paper should be adapted to carry out more similar tests, not only for PTL materials, but for MPLs, multiple layered GDLs, and CLs as well. The possibility to standardise the thermal conductivity change in a porous material due to hydrogen saturation based on the specifications of that material should also be examined. The effect of hydrogen saturation in porous PEMFC should also be tested thoroughly at different levels of humidity, as water, the product of the reaction in a PEMFC is also present in the MEA, raising the thermal conductivity of the porous regions even further.

The rig used in this thesis can be an important part of the further work in this field of study. A large capsule should be built to fit the whole rig inside. This should be done to minimise the chance of external influence to the rig during measurements. The capsule should have some sort of drain in the top where hydrogen can naturally drain from the capsule without causing a large draft, like in a fume hood. The fragile thermocouples should be thoroughly tested and then completely insulated and fastened to keep them safe from physical contact with anything or anyone managing the rig. The LabView should be further programmed in such a way that the results from the test are automatically calculated and all the necessary plots provided.

Chapter 7

Conclusions

This thesis has contributed to the understanding of heat management in the PEMFC by proving that by saturating a porous PEMFC GDL material with hydrogen, the total thermal conductivity of the GDL region increase due to the high thermal conductivity of the hydrogen gas. This is proven experimentally in this thesis by measuring the thermal conductivity in Freudenberg H1410 and Sigracet® 10BA PTL materials when saturated with air and hydrogen.

The thermal conductivity for Freudenberg H1410 increased by between 20 and 25 % respectively, depending on the compaction pressure. i.e. from a thermal conductivity of 0.10 ± 0.013 to 0.13 ± 0.013 W m^{-1} K^{-1} for air to a thermal conductivity of 0.13 ± 0.013 to 0.15 ± 0.017 W m^{-1} K^{-1} for hydrogen at compaction pressures 3 - 23 bar. The thermal conductivity in the Sigracet® 10BA PTL increased by 10 - 15 % respectively. i.e. from a thermal conductivity of 0.24 ± 0.017 to 0.39 ± 0.08 W m^{-1} K^{-1} for air to a thermal conductivity of 0.28 ± 0.007 to 0.43 ± 0.03 W m^{-1} K^{-1} for hydrogen at compaction pressures 3 - 23 bar. The Sigracet® PTL have a higher thermal conductivity and was, therefore, less affected by the hydrogen. Temperature profiles made in COMSOL proved that the change in thermal conductivity in the PTL region made a notable impact on the heat management in the PEMFC. They also proved the importance of including the thermal effect from the hydrogen gas in future models and simulations to strengthen the validity of the results from those models and simulations.

Bibliography

[1] UNFCCC. Kyoto protocol, 1997. Available at
    http://unfccc.int/kyoto_protocol/items/2830.php,
    Downloaded 20.12.2016.

[2] UNFCCC. Paris agreement, 2015. Available at
    http://newsroom.unfccc.int/paris-agreement/,
    Downloaded 20.12.2016.

[3] UNFCCC. Paris agreement - status of ratification, 2017. Available at
    http://unfccc.int/paris_agreement/items/9444.php,
    Downloaded 22.07.2017.

[4] O. Burheim, P.J.S. Vie, S. Møller-Holst, J. Pharoah, and S. Kjelstrup. A calorimetric
    analysis of a polymer electrolyte fuel cell and the production of H_2O_2 at the cathode.
    Electrochimica Acta, 55(3):935–942, 2010.

[5] K.F. Bjelde, O.N. Brønseth, K.L. Hatlen, and T. Jensen. Automatisation of
    Measurement Rig and Measurement of Thermal Conductivity of Gas Diffusion
    Layers in PEM-Fuel Cells. Bachelor's thesis, Norwegian University of Science and
    Technology (NTNU), Trondheim, Norway, 2016.

[6] O. Burheim, P.J.S. Vie, J.G. Pharoah, and S. Kjelstrup. Ex situ measurements of
    through-plane thermal conductivities in a polymer electrolyte fuel cell. *Journal of
    Power Sources*, 195(1):249–256, 2010.

[7] P.J.S. Vie and S. Kjelstrup. Thermal conductivities from temperature profiles in the
    polymer electrolyte fuel cell. *Electrochimica Acta*, 49(7):1069–1077, 2004.

[8] M. Khandelwal and M.M. Mench. Direct measurement of through-plane thermal
    conductivity and contact resistance in fuel cell materials. *Journal of Power Sources*,
    161(2):1106–1115, 2006.

[9] J. Ramousse, S. Didierjean, O. Lottin, and D. Maillet. Estimation of the effective
    thermal conductivity of carbon felts used as pemfc gas diffusion layers. *International
    Journal of Thermal Sciences*, 47(1):1–6, 2008.

[10] E. Sadeghi, N. Djilali, and M. Bahrami. Effective thermal conductivity and thermal contact resistance of gas diffusion layers in proton exchange membrane fuel cells. part 2: Hysteresis effect under cyclic compressive load. *Journal of Power Sources*, 195(24):8104–8109, 2010.

[11] E. Sadeghi, N. Djilali, and M. Bahrami. A novel approach to determine the in-plane thermal conductivity of gas diffusion layers in proton exchange membrane fuel cells. *Journal of Power Sources*, 196(7):3565–3571, 2011.

[12] P. Teertstra, G. Karimi, and X. Li. Measurement of in-plane effective thermal conductivity in PEM fuel cell diffusion media. *Electrochimica Acta*, 56(3):1670–1675, 2011.

[13] N. Zamel, E. Litovsky, S. Shakhshir, X. Li, and J. Kleiman. Measurement of in-plane thermal conductivity of carbon paper diffusion media in the temperature range of -20 °C to +120 °C. *Applied energy*, 88(9):3042–3050, 2011.

[14] N. Zamel, E. Litovsky, X. Li, and J. Kleiman. Measurement of the through-plane thermal conductivity of carbon paper diffusion media for the temperature range from +50 to +120 °C. *International Journal of Hydrogen Energy*, 36(19):12618–12625, 2011.

[15] O.S. Burheim, H. Su, H.H. Hauge, S. Pasupathi, and B.G. Pollet. Study of thermal conductivity of pem fuel cell catalyst layers. *International Journal of Hydrogen Energy*, 39(17):9397–9408, 2014.

[16] O.S. Burheim, G.A. Crymble, R. Bock, N. Hussain, S. Pasupathi, A. du Plessis, S. le Roux, F. Seland, H. Su, and B.G. Pollet. Thermal conductivity in the three layered regions of micro porous layer coated porous transport layers for the pem fuel cell. *International Journal of Hydrogen Energy*, 40(46):16775–16785, 2015.

[17] L. Cindrella, A.M. Kannan, J.F. Lin, K. Saminathan, Y. Ho, C.W. Lin, and J. Wertz. Gas diffusion layer for proton exchange membrane fuel cells—a review. *Journal of Power Sources*, 194(1):146–160, 2009.

[18] N. Zamel and X. Li. Effective transport properties for polymer electrolyte membrane fuel cells–with a focus on the gas diffusion layer. *Progress in energy and combustion science*, 39(1):111–146, 2013.

[19] The Engineering Toolbox. Thermal conductivity of common materials and gases, 1997. Available at `http://www.engineeringtoolbox.com/thermal-conductivity-d_429.html`, Downloaded 15.02.2017.

[20] J.H. Lienhard. *A Heat Transfer Textbook: Fourth Edition*. Dover Civil and Mechanical Engineering. Dover Publications, 2013.

[21] R Clausius. *Abhaudlungen iiber die mechanische Warmetheorie Friedrich Vieweg*. Braunschweig, 1864.

[22] F. Kreith, R.M. Manglik, and M.S. Bohn. *Principles of heat transfer*. Cengage learning, 2012.

[23] M.J. Moran, H.N. Shapiro, D.D. Boettner, and M.B. Bailey. *Principles of Engineering Thermodynamics - seventh edition, SI Version*. Wiley, 2012.

[24] P.W. Atkins and C.A. Trapp. *Solutions manual for physical chemistry*. Oxford [etc.]: Oxford University Press, 1994.

[25] L. Carrette, K.A. Friedrich, and U. Stimming. Fuel cells–Fundamentals and applications. *Fuel cells*, 1(1):5–39, 2001.

[26] H. Ibrahim, A. Ilinca, and J. Perron. Energy storage systems - characteristics and comparisons. *Renewable and sustainable energy reviews*, 12(5):1221–1250, 2008.

[27] J. Zhang. *PEM fuel cell electrocatalysts and catalyst layers: Fundamentals and applications*. Springer Science & Business Media, 2008.

[28] F. Seland, T. Berning, B. Børresen, and R. Tunold. Improving the performance of high-temperature pem fuel cells based on pbi electrolyte. *Journal of Power Sources*, 160(1):27–36, 2006.

[29] T.L. Yu, H. Lin, K. Shen, L. Huang, Y. Chang, G. Jung, and J.C. Huang. Nafion/ptfe composite membranes for fuel cell applications. *Journal of Polymer Research*, 11(3):217–224, 2004.

[30] M.M. Mench. *Fuel Cell Engines*. Wiley, 2008.

[31] G.H. Aylward and T.J.V. Findlay. *SI Chemical Data - 6th edition*. Wiley, 2008.

[32] O. Burheim, S. Kjelstrup, J.G. Pharoah, P.J.S. Vie, and S. Møller-Holst. calculation of reversible electrode heats in the proton exchange membrane fuel cell from calorimetric measurements. *Electrochimica Acta*, 56(9):3248–3257, 2011.

[33] D.A. Noren and M.A. Hoffman. Clarifying the butler–volmer equation and related approximations for calculating activation losses in solid oxide fuel cell models. *Journal of Power Sources*, 152:175–181, 2005.

[34] National Instruments. Labview software description, 2017. Available at `http://www.ni.com/en-gb/shop/labview.html`, Downloaded 03.07.2017.

[35] COMSOL. Introduction to comsol multiphysics 5.3, 2017. Available at `https://cdn.comsol.com/documentation/5.3.0.260/IntroductionToCOMSOLMultiphysics.pdf`, Downloaded 03.07.2017.

[36] G.E.P. Box, W.G. Hunter, and J.S. Hunter. *Statistics for experimenters: an introduction to design, data analysis, and model building*, volume 1. JSTOR, 1978.

[37] S. Weisberg. *Applied linear regression*, volume 528. John Wiley & Sons, 2005.

[38] D.M. Rowe. *CRC handbook of thermoelectrics*. CRC press, 1995.

[39] O.S. Burheim, J.G. Pharoah, H. Lampert, P.J.S. Vie, and S. Kjelstrup. Through-plane thermal conductivity of pemfc porous transport layers. *Journal of Fuel Cell Science and Technology*, 8(2):021013, 2011.

[40] Freudenberg Group. Freudenberg gdl product info, 2017. Available at `https://fuelcellcomponents.freudenberg-pm.com/products/gas-diffusion-layers`, Downloaded 20.06.2017.

[41] SGL Group. Sigracet® 10 product info, 2017. Available at `https://www.fuelcellsetc.com/store/DS/SGL-GDL_10.pdf`, Downloaded 20.06.2017.

[42] R. Taherian. A review of composite and metallic bipolar plates in proton exchange membrane fuel cell: Materials, fabrication, and material selection. *Journal of power sources*, 265:370–390, 2014.

[43] O.S. Burheim, H. Su, S. Pasupathi, J.G. Pharoah, and B.G. Pollet. Thermal conductivity and temperature profiles of the micro porous layers used for the polymer electrolyte membrane fuel cell. *International Journal of Hydrogen Energy*, 38(20):8437–8447, 2013.

# Appendices

Appendix A
LabView Code

The block diagram used to run the measurement rig used in this thesis, is depicted in Figs. A.1-A.3. The large block diagram is represented by three figures here, but it is really one block diagram. The while loop where temperature measurements are made and heat flow calculated is presented in Fig. A.1. The gas feed system, background log, and all plots shown on the front panel are programmed into that while loop. Figure A.2 depicts the while loop where the pressure management is programmed. The log output files used to calculate the results are also made there in 7 different subVIs. The block diagram of one of those subVIs is shown in Fig. A.3.
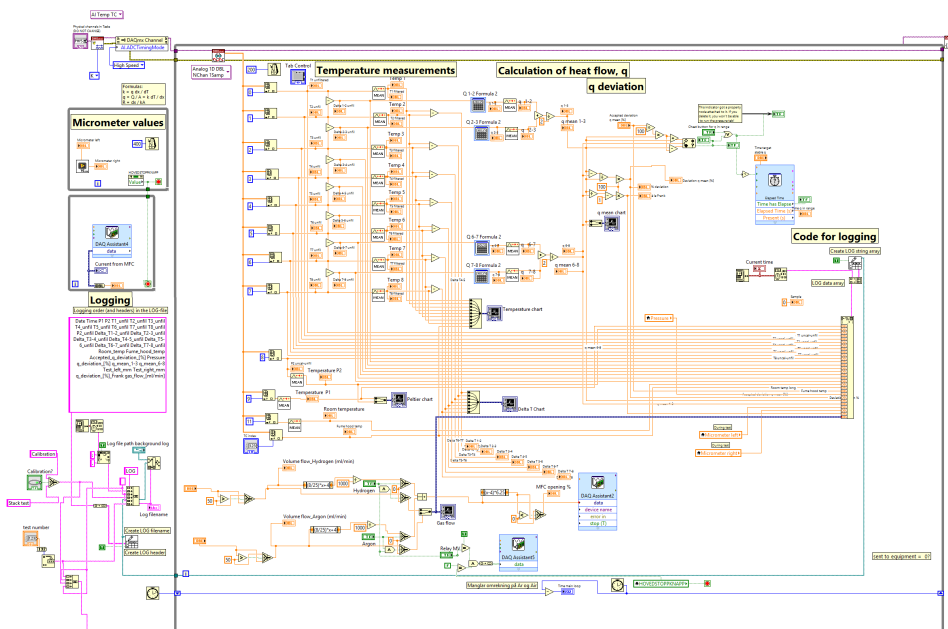
Figure A.1: Block diagram while loop, including programming for temperature measurements, a gas feed system, writing a background log, and all plots shown on the front panel.
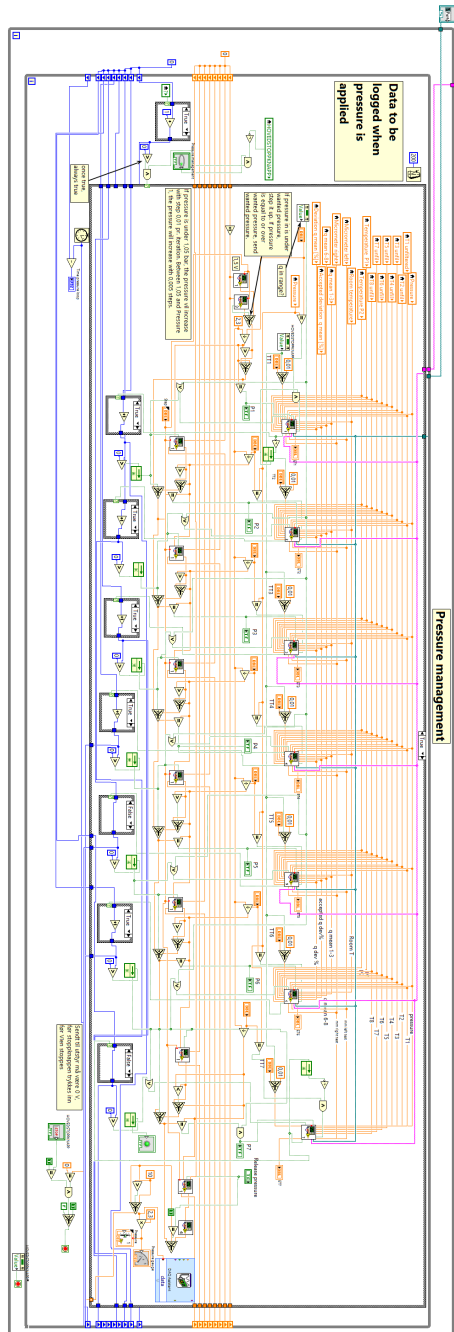
Figure A.2: Block diagram while loop for pressure management. The while loop makes sure the change in pressure is not to abrupt, keeping the rig from experiencing unnecessary mechanical stress.
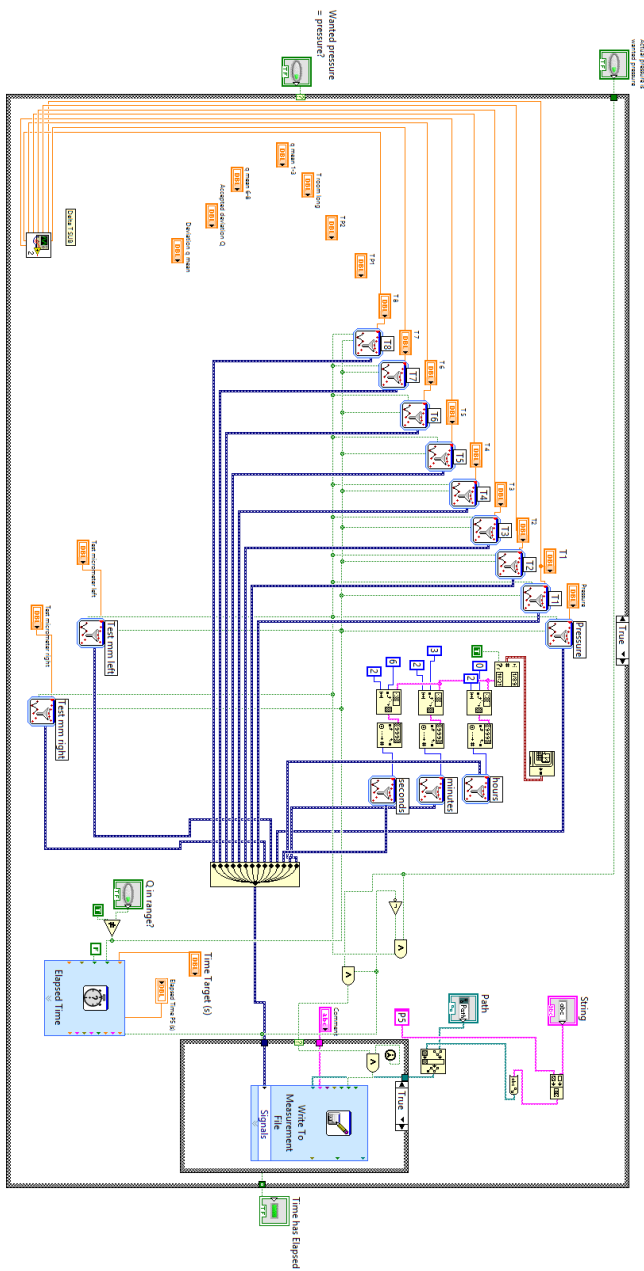
Figure A.3: One of seven subVI block diagrams used for collecting and logging data to be used in the results.
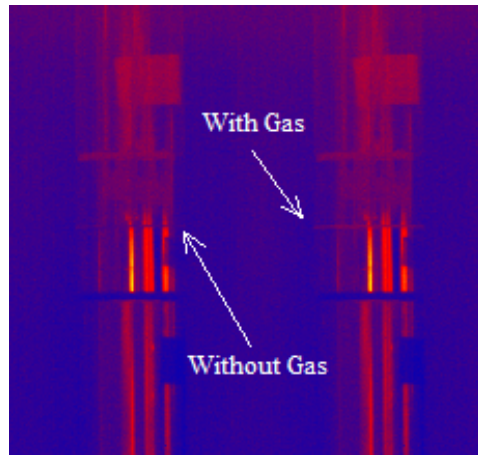
Appendix B
Thermal Camera

As a measure to be sure the gas fed to the rig was actually injected into the test sample, a thermal camera was used to film the rig and see where warm gas escaped. It was a worry that the thin sample would act like a plug for the gas at high pressures. The tightly compressed sample is more compact and could therefore stop the gas from flowing into it freely. A ToxiRAE Pro hydrogen gas detector from RAE systems (see Fig. B.1) was used to find any possible leaks from the gas flask to the rig. However, as hydrogen is a colourless and elusive gas, it was impossible to exactly measure if the gas escaped from the sample after it had saturated it or if it escaped from somewhere else on the rig.

Figure B.1: ToxiRAE Pro single gas detector set to detect hydrogen.

The accurate thermal camera Gobi-640-GigE form Xenics Infrared Solutions was therefore used to see where the gas escaped. Coupled to a computer, the camera was placed close to the rig. Live video feed from the camera was displayed on the computer where the temperature spectrum and colours to show temperature differences was chosen. It was possible to take snapshots of the video feed from the thermal camera in the computer program. The only place where a noticeable thermal change occurred when opening the gas valve was in the sample. This indicates strongly that the gas reaching the test rig also enters the test sample. Figure B.2 show the results from filming the sample with and without gas flowing through it. The colour red represents higher temperatures and blue lower temperatures. There are two images next to each other in the figure, one where the sample contains gas and one where it does not. The sample is visible as a thin line cutting the steel cylinder. The way the whole sample is a brighter red when gas is added to it indicates that the sample is completely saturated by the gas.

Figure B.2: Snapshot from thermal camera test. The sample saturated by warm gas is clearly visible as a red line. The sample without gas is visible as a cold blue line.

Appendix C
Stacking Peltier Modules

It was theorised that the measurement rig would be less affected by changes in the atmospheric conditions around the test rig if the heat flow through the cylinders and sample was greater. To make the heat flow greater a larger temperature difference had to be produced by the Peltier modules. The temperature in the sample was intended to be kept close to the atmospheric temperature, T_{atm}. However, the lower Peltier module generating T_{cold} was at maximum power. Therefore, the upper Peltier module could not generate a higher T_{hot} without altering the temperature of the sample.

A test was carried out to decide if T_{cold} could be lowered by coupling two Peltier modules in a series. A thermocouple was first fastened on each side of one Peltier module. The Peltier module was then introduced to different voltages. The same was done with two Peltier modules afterwards. A picture of the setup can be found in Fig. C.1. The Peltier modules was electrically coupled in parallel, but geographically in series. This meant that the cold side of the one of the Peltier modules would be in direct contact with the hot side of the other one. They would also be exposed to the same voltage.

Figure C.1: Two clamps clamp the two peltier modules together as well as a thermocouple on each outer side.

Table C.1 lists the results from the double Pelter test.

Table C.1: Peltier modules in series test.

Single Peltier module

[V]	[A module^{-1}]	[W module^{-1}]	T_{cold} [°C]	T_{hot} [°C]	ΔT [K]
0.00	0.00	0.00	26	26	0
1.00	0.43	0.43	24	29	5
2.00	0.83	1.66	23	35	12
3.00	1.20	3.60	22	41	19
4.00	1.51	6.04	26	51	25
5.00	1.82	9.10	28	59	31

Two Peltier modules in series

[V]	[A module^{-1}]	[W module^{-1}]	T_{cold} [°C]	T_{hot} [°C]	ΔT [K]
0.00	0.00	0.00	27	27	0
1.00	0.42	0.42	22	33	11
2.00	0.80	1.60	19	41	22
3.00	1.15	3.45	19	52	33
4.00	1.48	5.92	21	64	43
5.00	1.78	8.88	24	76	52

As seen in table C.1 a larger temperature drop is achieved without stressing the Peltier modules by setting them up in a series. T_{cold} increase when the modules are exposed to high power. this is not a problem as a cooling fan removes the heat from the hot side of the module. A colder hot side leads to an even colder cold side. After this test two Peltier modules was mounted in series to get a lower T_{cold} on the rig. This made it possible to increase the heat flow through the sample.
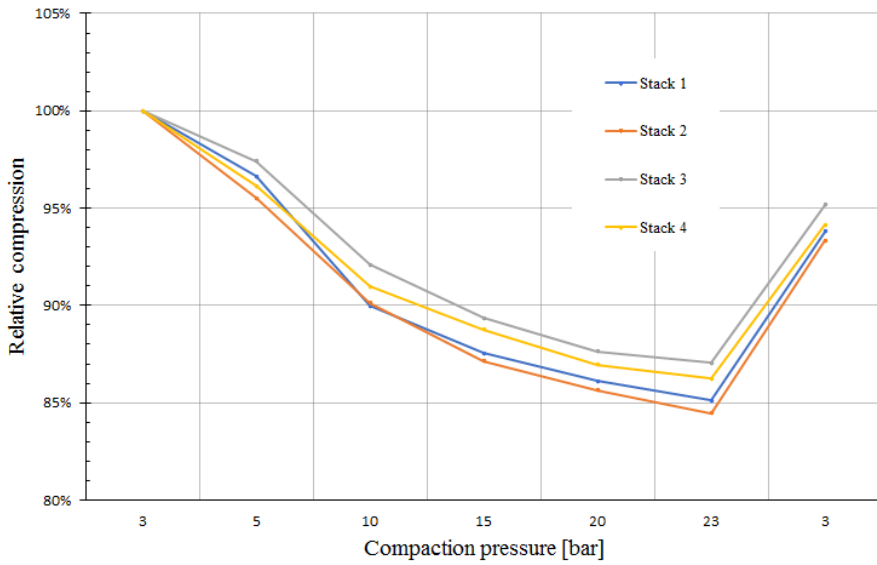
Appendix D
Relative Compression of Samples

Two types of PTL materials were tested in this thesis. Sigracet® 10BA and Freudenberg H1410 PTLs were cut into circular samples that were either tested one by one or gathered in a thicker stack and tested that way. The diameter of the samples was 21 mm and the thickness varied. In the test procedure, the samples were exposed to a through-plane temperature drop at different compaction pressures. The tests were performed with different gases present in the samples. However, this did not affect the compression of the samples. Each test started with a compaction pressure of 3 bar. The compaction pressure then went through several stages of compaction pressures up to the maximum of 23 bar, before dropping to the start value of 3 bar.

As two different materials were used in the testing, two figures have been prepared to show the relative compression of the samples/stacks. Table 4.1 describe the tested materials. An overview of the sample thicknesses measured during testing is found in Tab. D.1. In Figs. D.1 and D.2, a plot has been drawn to illustrate the compaction of the PTL materials relative to the thickness at the start of the test. When comparing the figures, it is easy to see that the Sigracet® PTL is much more compressible than the Freudenberg PTL. This was expected from the characteristics of the materials, but the difference is greater than expected. The permanent deformation is large for the Sigracet®. When releasing the pressure, the thickness is only 2/3 of the what it was at the start of the test. The Freudenberg PTL withstand the pressure better and suffer from only 5 % reduction in thickness after experiencing a compaction pressure of 23 bar.

Table D.1: Compression of Freudenberg H1410 and Sigracet® 10BA PTLs during testing.

	pressure [bar]	Freudenberg H1410		Sigracet® 10BA	
		thickness of stack [μm]	relative comp. [%]	thickness of stack [μm]	relative comp. [%]
1. stack	3	123.7	100.0	325.8	100.0
	5	119.5	96.6	318.5	97.8
	10	111.3	90.0	266.5	81.8
1 sample	15	108.3	87.5	226.5	69.5
in stack	20	106.5	86.1	199.6	61.3
	23	105.3	85.1	188.3	57.8
	3	116.0	93.8	210.5	64.6
2. stack	3	250.7	100.0	703.3	100.0
	5	239.5	95.5	664.5	94.5
	10	226.0	90.1	558.8	79.5
2 samples	15	218.5	87.1	472.0	67.1
in stack	20	214.8	85.7	410.8	58.4
	23	211.8	84.5	388.8	55.3
	3	234.0	93.3	435.8	62.0
3. stack	3	366.2	100.0	977.8	100.0
	5	356.8	97.4	924.9	94.6
	10	337.3	92.1	770.5	78.8
3 samples	15	327.3	89.4	654.3	66.9
in stack	20	321.0	87.7	576.5	59.0
	23	318.8	87.0	541.6	55.4
	3	348.5	95.2	614.0	62.8
4. stack	3	486.8	100.0	1219.8	100.0
	5	468.0	96.1	1164.3	95.4
	10	442.8	91.0	961.0	78.8
4 samples	15	432.0	88.8	809.5	66.4
in stack	20	423.3	87.0	708.3	58.1
	23	419.8	86.2	664.3	54.5
	3	458.3	94.1	759.7	62.3

Figure D.1: Relative compaction for the tested Freudenberg H1410 PTL material from the start at 3 bar compaction pressure, up to 23 bar, and down to 3 bar again.
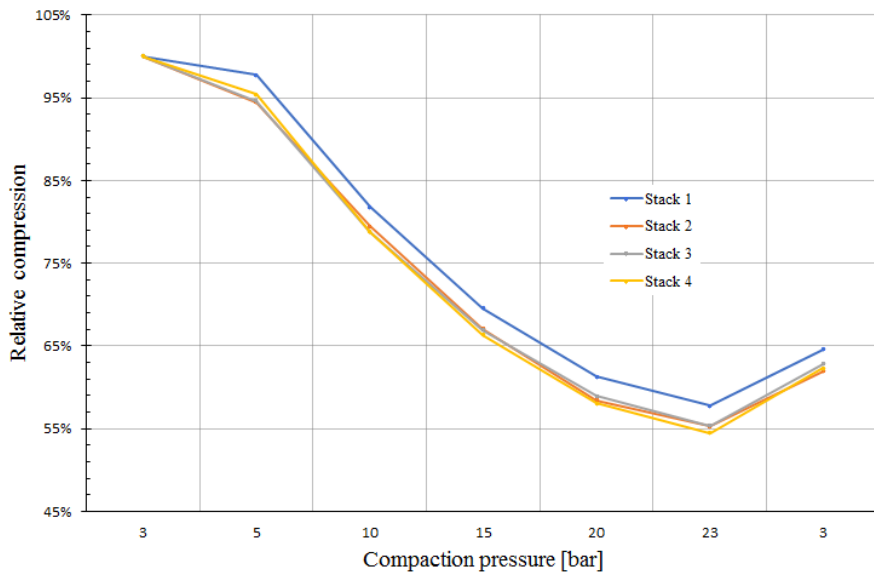
Figure D.2: Relative compaction for the tested Sigracet® 10BA PTL material from the start at 3 bar compaction pressure, up to 23 bar, and down to 3 bar again.